Nanoscale

ARTICLE

Janus plasmonic-magnetic gold-iron oxide nanoparticles as contrast agents for multimodal imaging

Received 00th January 20xx,
Accepted 00th January 20xx

DOI: 10.1039/x0xx00000x

www.rsc.org/

Javier Reguera,*[a,b,c] Dorleta Jiménez de Aberasturi,[a,b] Malou Henriksen-Lacey,[a,b] Judith Langer,[a,b] Ana Espinosa,[d] Boguslaw Szczupak,[a] Claire Wilhelm,[d] and Luis M. Liz-Marzán[a,b,c]

The design of compact nanoprobes for multimodal bioimaging is a current challenge and may have a major impact on diagnostics and therapeutics. Multicomponent gold-iron oxide nanoparticles have shown high potential as contrast agents in numerous imaging techniques due to the complementary features of iron oxide and gold nanomaterials. In this paper we describe novel gold-iron oxide Janus magnetic-plasmonic nanoparticles as versatile nanoprobes for multimodal imaging. The nanoparticles are characterized as contrast agents for different imaging techniques, including X-ray computed tomography (CT), T_2-weighted nuclear magnetic imaging (MRI), photoacoustic imaging (PA), dark-field and bright-field optical microscopy, transmission electron microscopy (TEM), and surface enhanced Raman spectroscopy (SERS). We discuss the effect of particle size and morphology on their performance as contrast agents and show the advantage of a Janus configuration. Additionally, the uptake of nanoparticles by cells can be simultaneously visualized in dark- and bright-field optical microscopy, SERS mapping, and electron microscopy. These complementary techniques allow a complete view of cell uptake in an artifact-free manner, with multiplexing capabilities, and with extra information regarding the nanoparticles´ fate inside the cells. Altogether, the results obtained with these non-invasive techniques show the high versatility of these nanoparticles, the advantages of a Janus configuration, and their high potential in multipurpose biomedical applications.

Introduction

The use of non-invasive imaging techniques is one of the current pillars of biomedicine for the early detection and screening of diverse pathologies, and their therapeutic treatment. *In vivo* imaging methods such as magnetic resonance imaging (MRI), X-ray computed tomography (CT), positron emission tomography (PET), single-photon emission computed tomography (SPECT), ultrasound (US), optical near infrared (NIR) imaging, or photoacoustic (PA) imaging are some of the most common techniques. Each of these techniques offers specific advantages, related e.g. to: spatial resolution, sensitivity, penetration depth, imaging time, ease of use, cost, or availability of the technique. This means that there is not a one-to-serve-them-all technique.[1-3] Such current limitations are usually overcome by making use of combinational imaging techniques (multimodal imaging) and contrast agents that improve their sensitivity and resolution.[1-5] Additionally, to gain further information about specific pathologies or therapeutic treatments, *in vivo* imaging requires complementary microscopy techniques (*in vitro* and *ex vivo* histology experiments) that provide sufficient information at the cellular level.

Nanomaterials have demonstrated unparalleled efficiency as contrast agents in various imaging techniques, thereby contributing to the advancement of this field. Their rapid expansion as contrast agents is mainly due to their unique, nanoscale-related properties, such as superparamagnetism, fluorescence, and plasmon resonances, together with slow diffusion times in biological media and easy surface functionalization for targeting and drug delivery.[1,6] Despite this progress, further advances in multimodal imaging require more complex nanoparticles that can act as contrast agents simultaneously in different techniques, *i.e.* which allow multimodal imaging with enhanced resolution, sensitivity, and functionality. From this point of view, multicomponent nanoparticles displaying combined nanomaterial properties are unique tools as main enablers of biomedical therapies. From the wide variety of currently available multicomponent nanoparticles, those made of gold and iron oxide have proven to be exceptional candidates for biomedical applications in general, and for multimodal imaging in particular. Among such properties, superparamagnetism in iron oxide nanoparticles stands out because it allows magnetic handling and targeting, magnetic hyperthermia, as well as contrast in T_2-weighted MRI.[7-9] Gold nanoparticles on the other hand display localized

[a] CIC biomaGUNE, Paseo de Miramón 182, 20014 Donostia-San Sebastián, Spain.
[b] Biomedical Research Networking Center in Bioengineering Biomaterials and Nanomedicine, Ciber-BBN, 20014 Donostia-San Sebastián, Spain.
[c] Ikerbasque, Basque Foundation for Science, 48013 Bilbao, Spain.
[d] Laboratoire Matière et Systèmes Complexes, UMR 7057, CNRS and University Paris Diderot, 75205 Paris Cedex 13, France.
Electronic Supplementary Information (ESI) available: [TEM images and characterization plots]. See DOI: 10.1039/x0xx00000x

surface plasmon resonances (LSPR), and intense light scattering. This plasmonic behavior renders them highly effective as contrast agents in dark-field optical imaging, valuable substrates for surface enhanced Raman scattering (SERS) detection, and efficient nanoheaters in photothermal therapies.[10,11] Furthermore, both gold and iron oxide are biocompatible and can be easily functionalized, thanks to the affinity of different chemical functional groups toward the nanoparticle surface, including thiols for gold, and catechols, silanes or diols for iron oxide, among others.

Diverse nanoparticle morphologies have been reported which combine gold with other nanomaterials, including not only iron oxide but also quantum dots, up-converting nanoparticles, and others.[12-15] In the case of gold-iron oxide nanoparticles, most of them correspond to core-shell iron oxide-gold structures,[16-23] but other morphologies include core-satellite,[24,25] heterodimers (also called dumbbells),[26-28] or larger polymeric and silica embedded assemblies.[29,30] Each morphology presents different features, including stability in biological media, easy access of water to the iron oxide surface that increases magnetic relaxivity, or higher magnetic or plasmonic activity. Aspects such as easy functionalization or compactness should also be taken into account toward biomedical applications. The use of compact nanoparticles prevents, for example, clearance through the liver and spleen and can help achieve higher penetration in cancer tissues while retaining structural integrity until the biomedical function is achieved.[1,15,22]

Janus nanoparticles (with two chemically different surface regions) have emerged as exceptional candidates toward many technological and biomedical applications. Their strong interaction with interfaces has been used e.g. to create emulsified nanoreactors, filtering nanomembranes, or block-copolymers with optical and electronic properties.[31,32] Other uses include: antireflecting surfaces, electronic displays, nanoswimmers, or as building blocks for more complex molecular colloids and supracrystals.[33-36] They offer extraordinary potential in biomedicine, as they can mimic natural biomolecules, have directed interactions with cell membranes, or offer regions with high concentrations of biofunctional molecules, while keeping multiple functionalities.[37-39]

Here we highlight the use of versatile magnetic-plasmonic Janus nanoparticles composed of an iron oxide nanosphere and a branched gold nanostar (hereafter called Janus magnetic nanostars), as contrast agents for multimodal imaging. The Janus character of these nanoparticles offers easy and selective functionalization of each side of the inorganic core. They further allow easy access of water to the iron oxide surface, contrary to core-shell nanoparticles, and, as opposed to simpler Janus dumbbell-like nanoparticles, they exhibit strong plasmonic activity with intense plasmon resonances in the NIR (first biological transparency window).[40,41] In addition, as described below, the strong plasmonic behavior and high stability in biological media can be preserved even when the size is as small as 25 nm. We evaluated in detail their magnetic and plasmonic properties to determine their multifunctional capabilities, and subsequently evaluated their properties as contrast agents in 3D tomography imaging techniques. This includes the determination of relaxivity constants in T_2 or spin-spin MRI as a function of nanoparticle morphology (iron oxide and gold nanostar relative sizes), the X-ray attenuation efficiency in CT as a function of gold content and X-ray energy, and the concentration and wavelength dependence in PA. Finally, analysis of cell uptake was used to evaluate the potential use of these nanoparticles as contrast agents in label-free dark- and bright-field optical imaging, TEM, and SERS imaging, thereby offering the possibility for barcode-like identification (multiplexing) of nanoparticle-loaded cells.

Results and discussion

Janus magnetic nanostars (JMNSs) were synthesized by modification of a recently reported method,[42] using two seed-mediated-growth steps. The synthesis starts with the formation of gold nanospheres that are used as seeds for gold-iron oxide nanodumbbells, which are subsequently used as seeds for the directional growth of asymmetric gold nanostars. In this work, the synthesis was simplified by addition of carboxyl-terminated-PEG to the nanodumbbells, rendering them soluble in *N*,*N*-Dimethylformamide (the solution in which nanostar synthesis takes place, see experimental section). This avoids difficulties related to phase-transfer of nanodumbbells, which are initially stabilized by oleic acid and oleylamine, into water.[7,43-45] Figure 1 shows representative TEM images corresponding to nanoparticles formed at different nanodumbbell seed concentrations (and constant amount of gold precursor). Varying this parameter, nanoparticles with average diameters ranging from ~20 nm to ~50 nm were readily synthesized (for clarity we named these nanoparticles as JMNS.XX.YY where XX and YY correspond to the average diameter of the iron oxide part and of the whole nanoparticle, respectively). Figure 1a shows representative TEM images of the different synthesized nanoparticles, comprising a 16 nm iron oxide domain and varying gold nanostar size. As the size decreases, it becomes easier to identify the iron oxide domains and we observe a decrease in the number of nanostar tips, reaching as few as 3-4 tips per nanoparticle for JMNS.16.25. If the amount of seeds added to the growth solution is largely increased, we reach a situation (JMNS.16.19) where only one or two “embryonic” tips are observed per nanoparticle, producing “L” or “T” shaped gold domains, rather than nanostars.

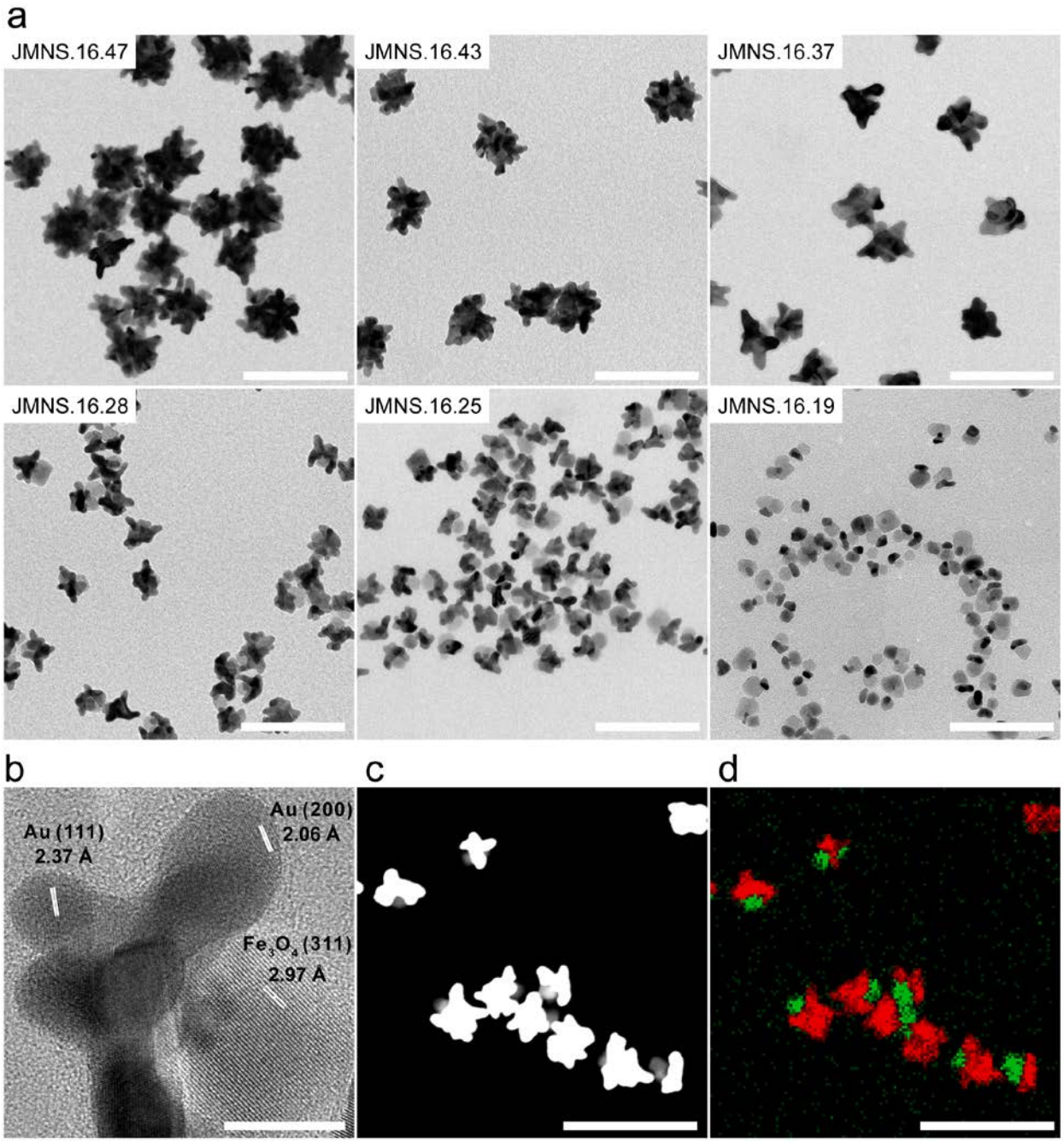

Figure 1. **a)** TEM images of different JMNSs obtained by varying the ratio of nanodumbbells-seeds to gold salt. As the nanoparticle size decreases, the iron oxide part (light grey) can be distinguished from the gold domain (dark grey or black). **b)** High resolution TEM image of a nanoparticle (JMNS.16.28) showing single crystal nanostar tips and Fe_3O_4. **c)** HAADF-STEM image of (JMNS.16.28), where gold appears white while iron oxide appears grey. **d)** EDX mapping of Fe (green) and Au (red) domains in (c). (Scale bars for (a), (c) and (d) = 100 nm; scale bar for (b) = 10 nm).

We also synthesized nanoparticles containing iron oxide domains with diameters up to 20 nm, by changing the gold-iron ratio in the dumbbell formation step, and used them to grow JMNSs of different sizes. Shown in the Supporting Information (SI) are TEM images for nanoparticles with three different sizes, JMNS.20.43, JMNS.20.41, and JMNS.20.36, which display similar morphologies to those presented in Figure 1.

Figure 1b shows a high resolution TEM image of a JMNS.16.28 nanoparticle where both components can be easily distinguished. The gold nanostar comprises single crystal tips, while the iron oxide corresponds to a single crystal sphere (or two crystal lobes in some cases) with the spinel lattice of iron oxide. X-ray photoelectron spectroscopy (XPS) analysis of the initial dumbbell seeds yields a Fe^{3+}/Fe^{2+} ratio of ca. 2.2 (see SI), indicating that most of the iron oxide corresponds to the magnetite (Fe_3O_4) phase. Finally, high-angle annular dark-field scanning electron microscopy (HAADF-STEM), and energy-dispersive X-ray (EDX) mapping of Fe and Au atoms, show a clear segregation of gold and iron in the two distinct nanoparticle domains (Figure 1 c-d). As we have previously demonstrated using EDX tomography the nanoparticles show

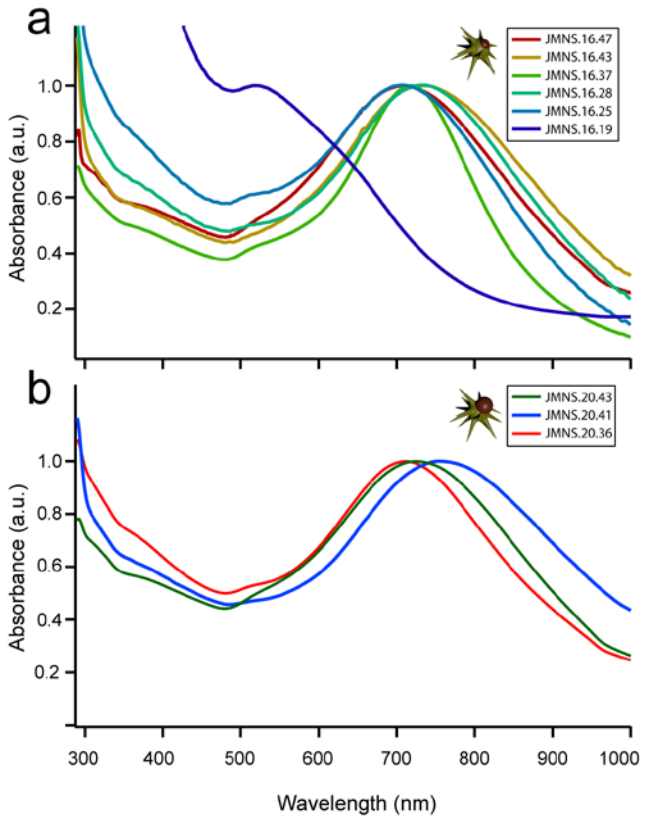

Figure 2. UV-Vis spectra of two sets of JMNSs obtained by varying the synthesis parameters. **a**) Nanoparticles with a 16 nm iron oxide domain and different gold nanostar sizes, the average total size ranging from 19 to 47 nm. **b**) Nanoparticles with a 20 nm iron oxide domain and different gold nanostar sizes, the average total size ranging from 36 to 43 nm.

Janus character, independently of the size of the gold part.[42]

The resulting nanoparticles show well-defined LSPR bands (Figure 2a) in the NIR around 700-800 nm, corresponding to a tips-body hybridized plasmon mode,[46] and a smaller band (shoulder) around 500-600 nm corresponding to the nanostar body. Bigger nanoparticles show in general red-shifted LSPRs, likely due to an increased aspect ratio of the nanoparticle tips. It should be noted that the largest nanoparticles, JMNS.16.47, fall out of the trend, most probably due to secondary nucleation (and increased polydispersity), which leads to a LSPR blue-shift. We found that the smallest JMNSs that still exhibit strong LSPR intensity in the NIR are the 25 nm nanoparticles. Below that size, *i.e.* JMNS.16.19, complete nanostars are not formed, so that only a broad and low intensity band is observed around 600-700 nm, while the band at 500-600 nm dominates. Similar NIR absorbance at 700-800 nm was observed for nanoparticles containing 20 nm iron oxide cores (Figure 2 b), with red-shifted LSPR when increasing particle size, up to certain size where polydispersity increases (see Table 1 and lower magnification TEM images in the SI).

In the case of nanodumbbells, the LSPR peak is centered around 550 nm (far from the NIR region) and is strongly damped by the presence of iron oxide.[47] Moreover, the growth of the larger gold domain, using polyvinylpyrrolidone (PVP) as surfactant, provides the nanoparticles with high stability in water, PBS, and cell media. The heterodimers can thus be readily transferred from non-polar organic solvents into water. Despite the high colloidal stability, slow reshaping (or tip rounding) was observed for most samples, as previously reported for other gold nanostar systems.[48,49] Reshaping was however dependent on particle size. For example, after ~6 months in aqueous solution, the reshaping of JMNS.16.37 and JMNS.20.41 was not perceptible in TEM and the LSPR band was blue-shifted by only 20 and 18 nm, respectively. However, for JMNS.16.25 TEM images showed some aggregation and significant reshaping into a spheroidal shape, while JMNS16.19 showed complete aggregation.

The magnetic properties of the nanoparticles, before and after growing the gold nanostars (nanodumbbells and JMNSs), were studied for two different sizes. Figure 3 shows the magnetization, M(H) and M(T) plots, of the nanodumbbells used as seeds (with iron oxide diameters of ~16 nm (a.1 and a.2) and ~20 nm (b.1 and b.2), ND.16 and ND.20, respectively). None of the nanodumbbells showed remanence or coercivity (see insets in a.1 and b.1), as expected for superparamagnetic nanoparticles. After gold nanostar growth (JMNS.16.25, and JMNS.20.41), the superparamagnetic behavior was maintained (Figure 3, a.3 and b.3). Analysis of the normalized magnetization M/Ms (H), according to the Langevin model (model explained in SI), yields a size distribution centered around 13.5 nm for ND.16 and 15.5 nm for JMNS.16.25, in both cases close to the size measured by TEM (16.2 ± 2.8 nm). The same behavior can be observed for JMNSs containing 20 nm iron cores. In this case, the Langevin approach yields a mean size of 19.9 nm for (ND.20) and 18.3 nm (JMNS.20.41), again in good agreement with the size measured using TEM (20.5 ± 4.0 nm) (the fitting of the plots is presented in the SI). Magnetic characterization was carried out by using highly dilute samples, in which the low iron oxide concentration makes it difficult to extract precise values for some magnetic parameters, such as the saturation magnetization. In general, the saturation magnetization of the tested nanoparticles ranged from 45 to 70 emu/g-$_{Fe}$, which is within the usual range reported in the literature for iron oxide nanoparticles.[24,26-28,50,51]

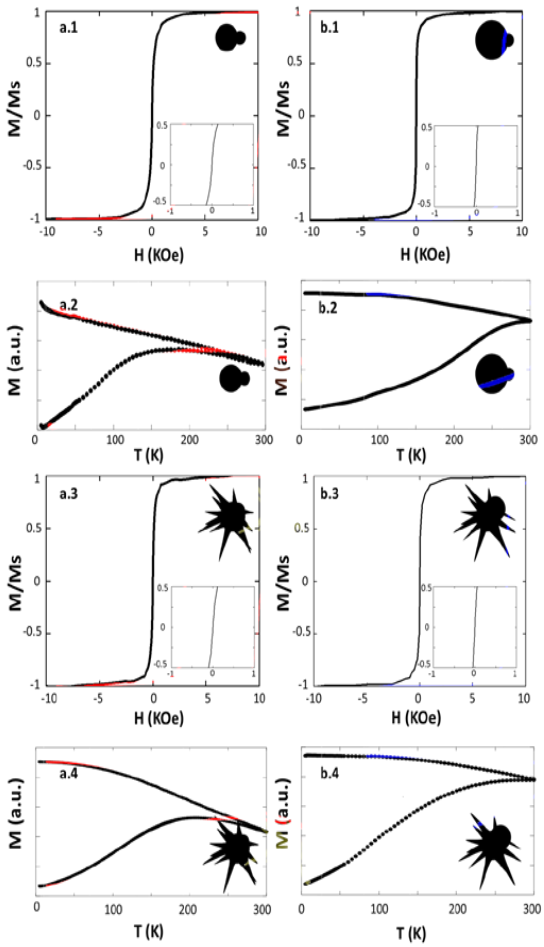

Figure 4. Hysteresis loops measured at room temperature and ZFC–FC curves for nanodumbbells and JMNSs with two different iron oxide sizes. a.1 and a.2 correspond to ND.16; a.3 and a.4 to JMNS.16.25, both with an iron oxide diameter of ~16 nm. b.1 and b.2 correspond to ND.20; b.3 and b.4 to JMNS.20.41, with ~20 nm iron oxide part. Magnetization was normalized to the saturation value (reduced magnetization) for the sake of comparison and quantitative analysis.

M(T) measurements were conducted using the Zero Field Cooling-Field Cooling protocol (ZFC/FC). As shown in Figure 3, a.2 and a.4 for JMNS.16 and JMNS.16.25, respectively, only minor changes in the magnetic properties were observed as a consequence of growing gold tips. The maximum of the ZFC line is rather wide in both cases, reflecting a moderately broad size distribution, as well as some degree of interparticle coupling. Under these conditions, the small mismatch between samples with and without gold tips is likely related to variations of randomly distributed local dipolar interactions. This can be confirmed to some extent by performing a fit of the experimental data in the framework of a model for non-interacting single magnetic domains, which includes the intrinsic temperature dependence of the effective anisotropy (see SI for details). Using this approach and assuming that the magnetization of iron oxide nanoparticles is around 400 emu/cm^3,[51] the theoretical curves correspond to average particle sizes of 15 nm, in good agreement with the hysteresis curves and TEM analysis. Moreover, the values of the effective anisotropy constants at room temperature (RT) K_{eff} hardly change before and after growth: $K_{eff\_ND.16}$= 18.6 KJ/m^3 (RT); $K_{eff\_JMNS.16.25}$= 17 KJ/m^3 (RT). The same discussion applies to

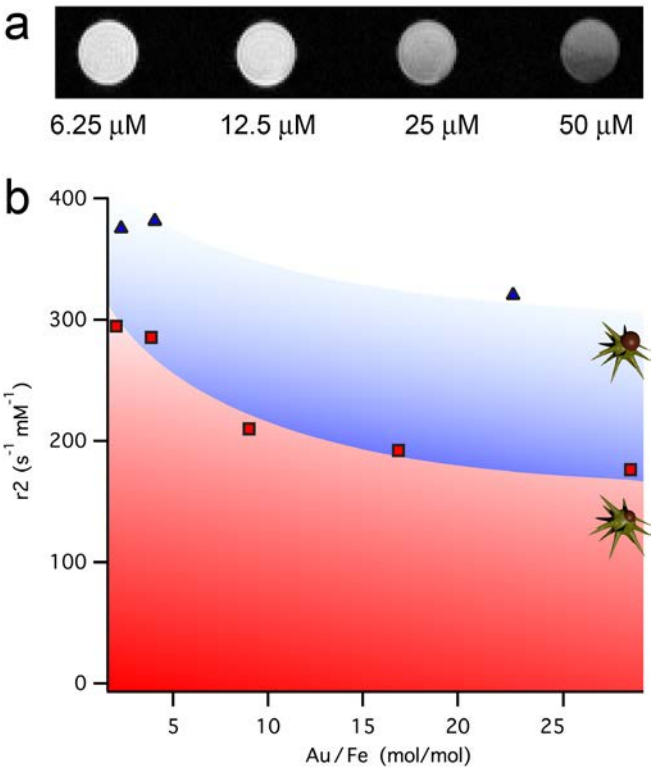

Figure 3. Effect of JMNS morphology on r_2 relaxivity values. **a)** MRI images of phantoms of aqueous solutions at different concentrations of JMNS.16.28, showing the variation in T_2 negative contrast. **b)** Measurement of relaxivities for nanoparticles with iron oxide components of 16 nm (in red), and 20 nm (in blue) and different sizes of the gold nanostar component, plotted as a function of gold-to-iron ratio in the nanoparticles. Red symbols correspond to JMNS.16.25, JMNS.16.28, JMNS.16.37, JMNS.16.43 and JMNS.16.47; blue symbols correspond to JMNS.20.36, JMNS.20.41 and JMNS.20.43. (The two colored regions have been included only to help the description of the trend and don't correspond to a model fit)

samples comprising larger iron oxide particles, i.e. ND.20 and JMNS.20.41, which exhibit a higher blocking temperature and a calculated average size of ~ 19.5 nm, also in agreement with TEM (20.5 ± 4 nm). The effective anisotropy constants at RT (K_{eff}) remain similar: $K_{eff\_ND.20}$= 18 KJ/m^3 (RT) and $K_{eff\_JMNS.20.41}$= 13 KJ/m^3 (RT). We also observed that the ZFC of JMNS.20.41 becomes a little wider and smoother than that for ND.20, likely due to stronger interparticle interactions.

Overall we can conclude that, iron oxide nanoparticles remain virtually unchanged after growing Au tips on nanodumbbells, and importantly, their superparamagnetic properties are maintained, thereby enabling e.g. magnetic purification without permanent magnetic aggregation, as well as magnetic targeting.

Magnetic resonance imaging

Iron oxide nanoparticles are known to be excellent negative contrast agents in spin-spin T_2 weighted MRI, due to the high magnetic field heterogeneities created at the protons of water molecules located close to the nanoparticles surface.[52-54] The r_2 relaxivities produced by our JMNSs were calculated *via* measurement of relaxation times at different concentrations ($1/T_2$ vs. [Fe] plots are shown in SI). Figure 4 and Table 1 show the relaxivity values obtained for JMNSs with 16 nm (red) and

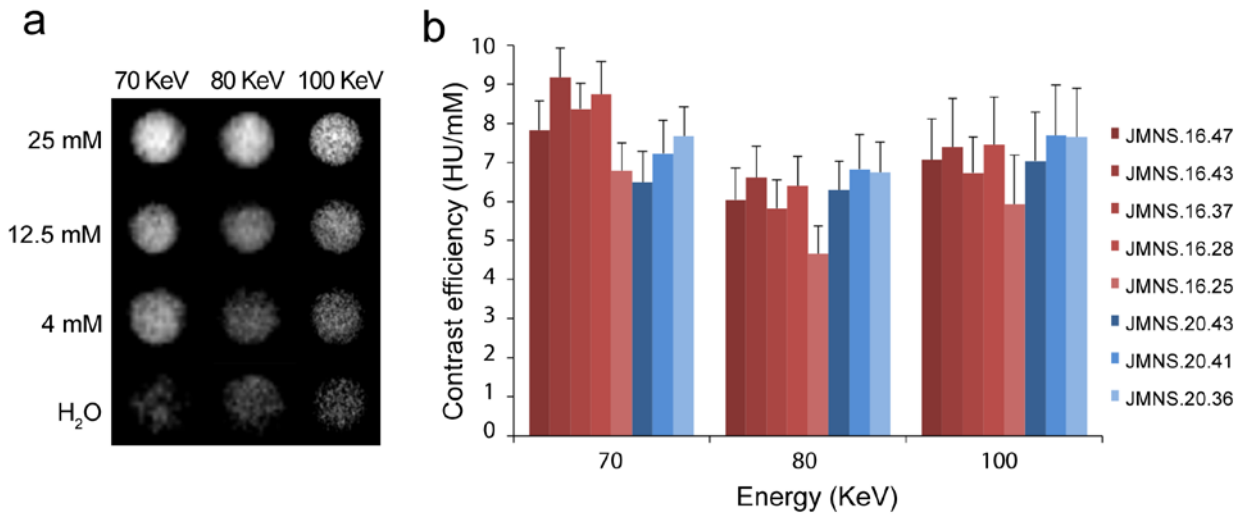

Figure 5 **a**) Images of phantoms containing nanoparticles (JMNS.16.28), at different concentrations and X-ray energies. **b**) CT contrast efficiency (in Hounsfield unit per Au concentration in mM) of different JMNSs (as labeled on the right) at three different X-ray energies.

20 nm (blue) iron oxide domains. The nanoparticles with smaller iron oxide parts yield high values of r_2 between ~180 and ~300 $s^{-1}mM^{-1}$. Relaxivity was found to increase with decreasing particle size, with a more pronounced variation for smaller nanoparticles (low [Au]/[Fe] ratio), whereas an almost constant value was determined for larger nanoparticles. An increase in relaxivity was observed for nanoparticles with larger iron oxide domains, reaching values of ca. 300-400 $s^{-1}mM^{-1}$, with a similar decrease for increasing gold nanostar domains.

We additionally noted that nanoparticles with 16 nm iron oxide cores induced higher relaxivity values than those for most commercially available iron oxide nanoparticles, used in clinical MRI (for example, Ferrumoxytol has a r_2 of 89 $s^{-1}mM^{-1}$, Ferridex 120 $s^{-1}mM^{-1}$, Ferumoxtran-10 65 $s^{-1}mM^{-1}$, and Resovist 38 $s^{-1}mM^{-1}$, when measured at 1.5 T), and in line with the best non-doped iron oxide nanoparticles.[7,50] It should be mentioned that such high relaxivity values are likely related to their Janus character, which allows closer access of water molecules to the iron oxide surface. In this regard, the initial growth of the gold part removes many water molecules from the vicinity of the iron oxide surface, thereby decreasing relaxivity. As the nanostars grow farther away from the iron oxide surface in a Janus conformation, removal of the closest water molecules decreases, resulting in much lower relaxivity attenuation.

Figure 4 also shows that the r_2 value increases with the size of the iron oxide domain, likely due to the increase in saturation magnetization with particle size. An enhancement around 100 $s^{-1}mM^{-1}$ is observed for 20 nm iron oxide nanoparticles, as compared to those with 16 nm. A further increase is expected for bigger iron oxide components, but this could be limited by the loss of superparamagnetism, which would give rise to magnetic aggregation due to permanent magnetization upon exposure to a magnetic field. Finally, although iron oxide nanoparticles are good T_2 contrast agents, they also produce a change in T_1, presenting an r_1 relaxivity around 6-14 $s^{-1}mM^{-1}$, which decreases with increasing gold nanostar size. The r_2/r_1 ratio shows a slight increase, with values around 20-30 and 40-50, for 16 and 20 nm iron oxide containing nanoparticles, respectively (see Supporting Information, and Table 1).

Therefore, optimization of these nanoparticles as MRI T_2-weighted contrast agents requires small gold nanostars and large the iron oxide part, for a higher r_2 relaxivity. However, the lower size limit is restricted by decreased stability and loss of plasmonic activity in the NIR when decreasing nanostar size (JMNS.16.19 shows low stability under a magnetic field), as well as by the loss of superparamagnetism above a certain diameter of iron oxide.

Computed tomography

Gold nanoparticles have been shown to serve as excellent contrast agents for X-ray attenuation in CT imaging. They produce higher attenuation than the current iodine-based standards, due to their higher atomic number and electron density.[55] They also show slower diffusion, thereby increasing the measurement time window, low toxicity, and easy surface functionalization for targeting, labeling or drug delivery.[55-57] To test the efficiency of JMNSs as CT contrast agents we used phantoms containing nanoparticle solutions at different concentrations and three different X-ray energies. Attenuation coefficients were calculated as the slope of the plot of attenuation vs. concentration.

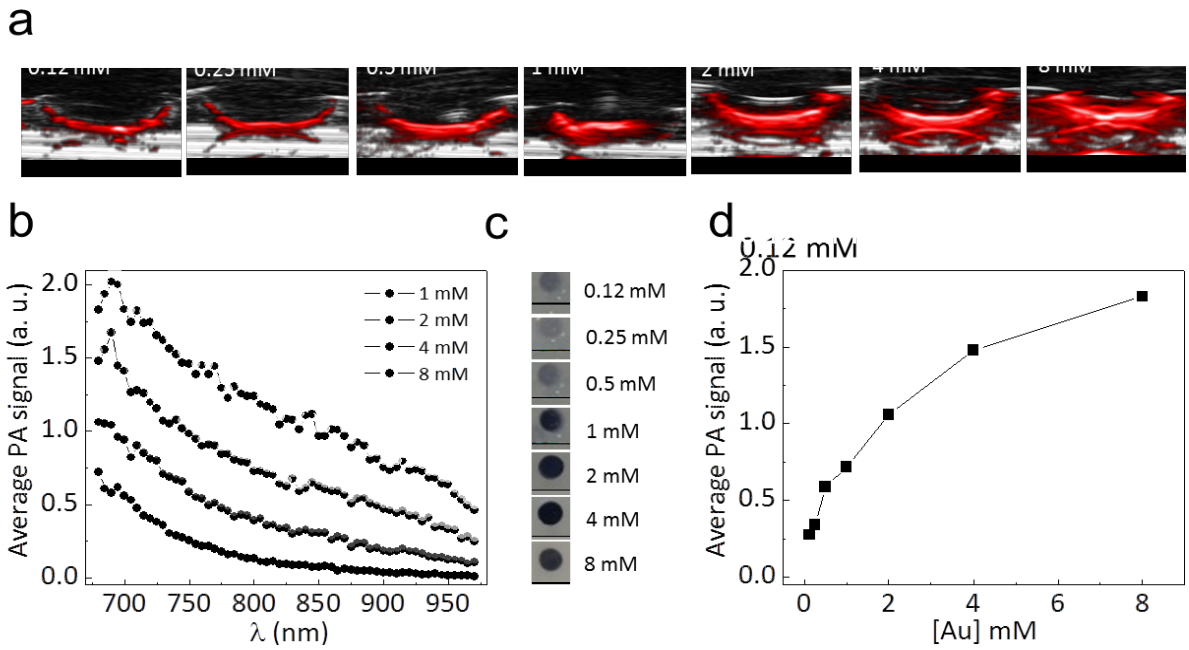

Figure 6. Photoacoustic imaging using JMNS.16.37 nanoparticles as PA contrast agents. **a)** Profile view of combined ultrasound and photoacoustic images of phantoms wells (30 µL of volume) containing nanoparticle agarose solution at different gold concentrations (from 0.12 to 8 mM, left to right). **b)** Average photoacoustic signal as a function of wavelength and nanoparticle concentration. **c)** Representative top-view images of phantoms of JMNS.16.37 agarose solutions. **d)** Photoacoustic signal at the maximum of signal (680 nm) and as a function of gold concentration (from 0.12 to 8 mM).

Figure 5a shows the change in contrast, as the nanoparticle concentration was increased. The contrast efficiency, or change in attenuation with contrast efficiency is shown in Figure 5b for the different nanoparticles. The highest attenuation was obtained at 70 keV, producing contrast efficiencies around 8 $HUmM^{-1}$. The lowest coefficients, around 6 $HUmM^{-1}$, were obtained at 80 keV, increasing again up to ~7 $HUmM^{-1}$ for the highest energy of 100 KeV. These results are in agreement with the attenuation produced by gold, which in general decreases with X-ray energy. However, a leap in attenuation is produced above the *K*-shell absorption edge at 80.7 KeV, which agrees with the attenuation increase from 80 to 100 KeV. Only small differences are appreciated for different nanoparticles, with no clear trend, in agreement with previous studies indicating that the size and shape of gold nanoparticles hardly affect X-ray attenuation.[56] Therefore, the small differences seen here could be due to experimental errors in ICP and CT measurements, and a negligible influence of the iron oxide domain.

The experimental values are of the same order as those previously reported in the literature.[55] The concentrations required to achieve a significant contrast are in general much higher than those needed for MRI (in the mM range for CT vs. the µM range for MRI). We thus conclude that, a high gold to iron ratio is beneficial in dual imaging applications, where both CT and MRI are used. As mentioned above, relatively high r_2 values are still obtained for big JMNSs, whereas smaller sizes are preferred for slower diffusion of nanoparticles in biological systems, meaning that a compromise is needed between the gold to iron ratio and the total nanoparticle size.

Photoacoustic imaging

Photoacoustic imaging (PA) has emerged as an exceptional non-invasive and real-time imaging technique that combines ultrasonic detection with optical imaging, thereby yielding both high spatial resolution and sensitivity.[58-60] The PA mechanism involves the absorbance of visible or NIR light by the tissue, resulting in adiabatic expansion after light-heat transduction, which induces photoacoustic signals. Although several endogenous contrast agents exist - such as hemoglobin, melanin, lipids or water – and can be used to produce a PA image, the use of exogenous contrast agents can highly increase detection depth and sensitivity.[58] For example, PA of nanosized contrast agents has been used in the detection of breast cancer at a depth of 31 mm below the surface.[61] In combination with the targeting capabilities of nanomaterials, the functionality of PA imaging can be largely increased.

Gold nanoparticles are excellent contrast agents for PA, as they show efficient photothermal conversion at the LSPR, while avoiding the photobleaching problems of dye molecules. Nanostars are particularly well suited for PA because they display a strong LSPR in the NIR, as well as excellent photothermal conversion.[62,63] As compared to nanodumbbells, the growth of nanostar tips is a significant advantage because the nanoparticle adsorption window is red-shifted, thereby avoiding the strong absorption by biological tissue in the visible. We thus tested the suitability of JMNSs as contrast agents in PA imaging. Figure 6a shows combined ultrasound and photoacoustic images of phantom wells (profile view) containing a nanoparticle agarose solution of JMNS.16.43 nanoparticles at different concentrations (from [Au] = 0.12 to 8

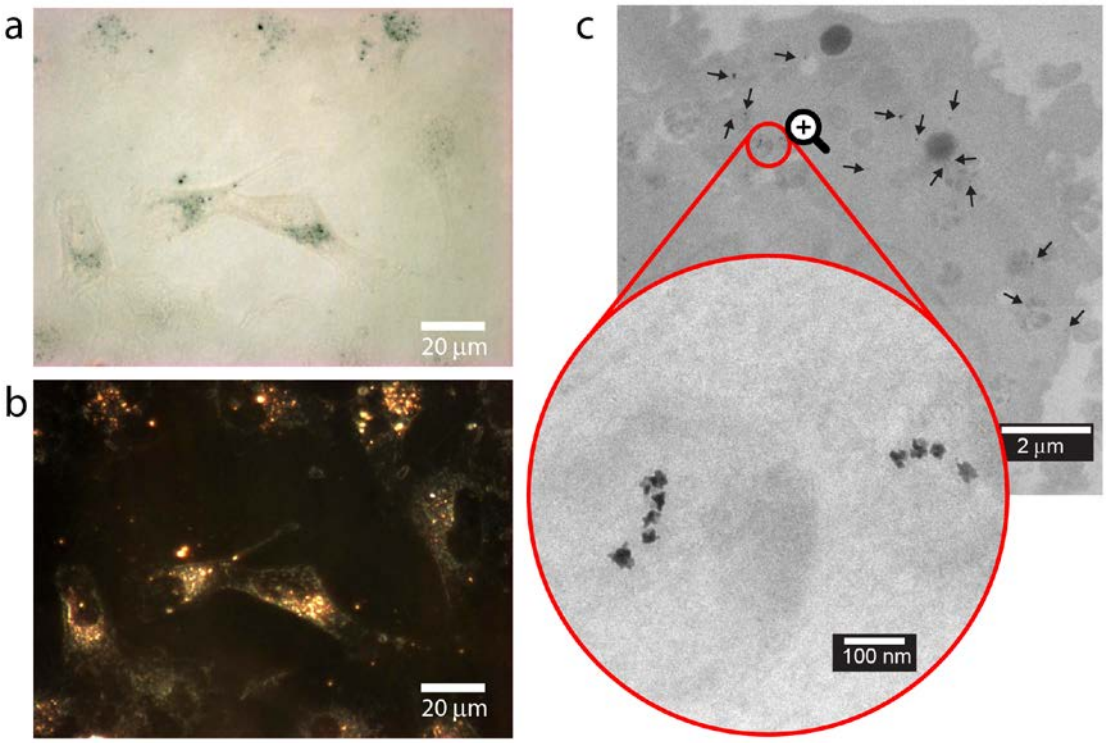

Figure 7. Cell imaging after incubation of an A549 cell culture with JMNS.16.28 nanoparticles. **a**) Bright field imaging after Prussian blue staining of the iron oxide component of the nanoparticle. Nanoparticles appear as blue-green spots within the cytoplasm of neutral red stained cells. **b**) Dark field imaging showing scattering of the gold nanostar components, which appear as bright spots inside the cells. The lack of nanoparticles in the nuclei is indicative of nanoparticle uptake rather than nanoparticle attachment to the cell surface. **c**) TEM images showing the nanoparticles as dark spots inside a cell due to the high contrast of Au. Arrows indicate where the nanoparticles are located. The zoomed image shows the uptake of small clusters of nanoparticles in endosomes. The iron oxide component of the nanoparticles can be distinguished in some of the nanoparticles, indicating high intracellular stability.

mM, top-view images of the wells at those concentrations are displayed in Figure 6c). In general, high contrast is observed for the concentrations tested. The variation of the PA signal as a function of wavelength is in agreement with the absorbance of the nanoparticles, with a maximum around 700 nm (Figure 6b). When the averaged signal is plotted as a function of concentration, a steep slope is obtained at low concentrations, representing a good sensitivity at 0.1-0.2 mM concentrations (Figure 6d). When increasing JMNS concentration, the slope is found to decrease, indicating signal saturation. This high contrast is related to the high photothermal conversion efficiency of these nanoparticles (e.g. JMNS.16.43 has a specific absorption rate of ~10 KW/g irradiated at 0.3 W/cm^2, λ = 680 nm) and opens up the possibility of simultaneous photothermal therapy and photothermal imaging in an eventual theranostic system. When the different tomography techniques are compared we can observe that the concentration required to obtain high contrast needs to be higher than that used for MRI (between one and two orders of magnitude), but lower than that for CT (one order of magnitude). Taking into consideration that the concentration is expressed in terms of the concentrations of Fe (MRI) and Au (CT and PA), a high [Au]/[Fe] ratio is convenient for combined multimodal imaging.

Optical and electron cell microscopy

3D tomography imaging techniques offer highly valuable information. However, these techniques usually require additional information to help identifying the biokinetics and nanomaterial/drug cell interaction. To this purpose, optical and electron microscopy studies are frequently performed *in vitro* or *ex vivo*, using cell cultures or histological tissues. Therefore, it is highly beneficial that the nanoparticles used for 3D imaging could also serve as contrast agents in the different microscopy modalities.

Cell uptake of JMNSs was first analyzed by label-free optical imaging, taking advantage of both the iron oxide and gold domains. Compared to fluorescent labeling, this system does not suffer from quenching by nanoparticles and possible artifacts or false labeling due to the detachment of fluorescent ligands. Figure 7a shows A549 bronchial epithelial cells after incubation with a dispersion of JMNS in cell medium. Cells were fixed and Prussian blue staining was applied to localize iron containing nanoparticles. Again, the morphology of the nanoparticles with an exposed iron oxide part, rather than a complete gold shell, facilitates the reaction of potassium ferrocyanide with iron atoms, giving rise to blue staining of the sample where the nanoparticles are located. Additionally, gold nanostars can be easily visualized under dark-field illumination, taking advantage of their high scattering coefficient at wavelengths around the surface plasmon resonance of the nanoparticles.[64,65] Figure 7b shows a dark-field image of the same area as in Figure 7a, where the gold

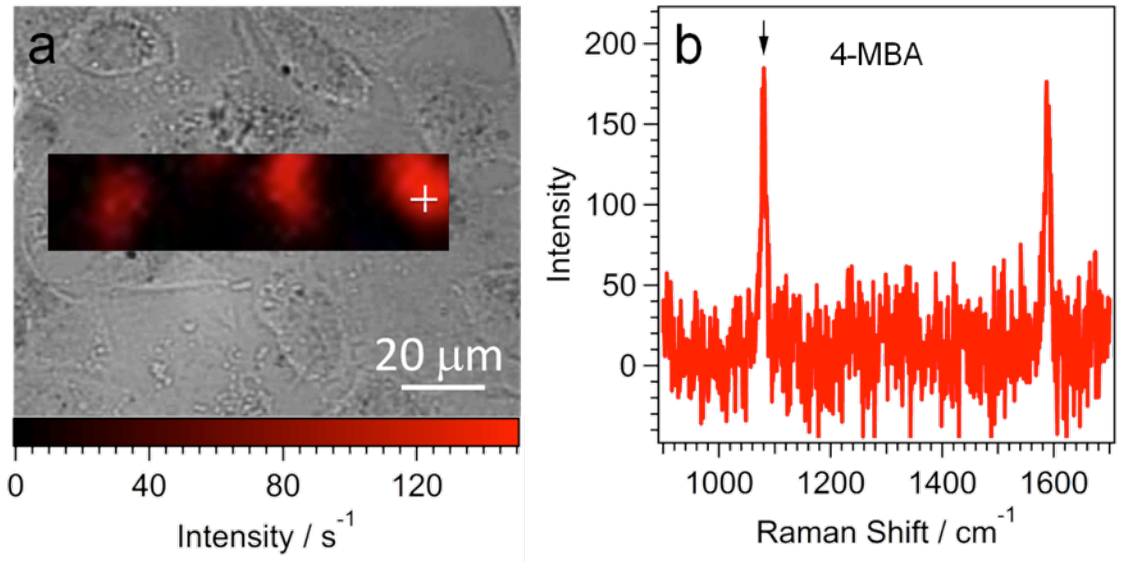

Figure 8. **a)** SERS image of A549 cells after incubation with 4-MBA labeled JMNS (4-MBA-JMNS.16.28). The SERS image is based on the Raman peak of 4-MBA at 1078 cm^{-1}, see signal labeled with black arrow in (b), and is presented as an inset on the optical microscopy image. **b**) SERS spectrum of the pixel inside the cell indicated by the white cross in (a).

nanostars in the JMNSs can be seen as bright gold-colored spots. Despite the small size of the nanoparticles used (28 nm), the scattering properties of branched gold nanoparticles[66] allow us to identify nanoparticle uptake in cells and to be distinguished from background scattering derived from the cell itself.

From the analysis of both images, it can also be observed that there is an excellent co-localization of the iron and gold domains of the nanoprobes (blue and bright spots corresponding to iron and gold probes, respectively). This is indicative of the high stability of JMNSs, their two components remaining together during cell experiments. Such high stability was also observed during nanoparticle purification, in which nanoparticles remained stable even under strong sonication. Since optical images clearly suggest endocytosis of nanoparticles by cells, we conducted TEM analysis of fixed cells to verify their intracellular location. Figure 7c shows a representative example of an A549 cell with endocytosed JMNSs, in which both iron oxide and gold nanostar parts of the nanoparticles can be distinguished. No JMNSs were seen at cell membranes and cell staining indicates endosomal uptake.

SERS mapping

SERS imaging has been recently introduced as a promising tool to identify the fate of nanoparticles in biomedical assays. The use of different cell tags allows a "barcode" labeling of gold nanoparticles (each molecule has a unique SERS fingerprint), thereby enabling the identification of different nanoparticles in multi-nanoparticle systems or multiplexing.[67-69] Additionally, and in contrast to fluorescent labeling, the Raman signal is dramatically quenched when the ligand is detached from the nanoparticle surface, thereby preventing the possibility of imaging artifacts. Anisotropic gold nanoparticles such as nanotriangles, nanorods and nanostars have all been shown to be excellent nanoprobes for SERS due to the presence of intrinsic hot spots at sharp tips and edges.[70,71] Nanostars in particular have attracted much interest for SERS bio-imaging, due to tunable LSPR bands in the NIR, thus matching the biological transparency window.[72,73]

To test the potential of JMNSs for SERS imaging, the nanoparticles were functionalized with the Raman reporter 4-mercaptobenzoic acid (4-MBA). This standard molecule attaches covalently to the gold surface (thiolated bond), does not compromise the colloidal stability of the nanoparticles and hamper nanoparticle aggregation due to its deprotonated state at neutral pH (negative charges of carboxylate groups). A549 cells were subsequently incubated with functionalized JMNSs, 4-MBA-JMNS.16.28, washed and then imaged by Raman microscopy by recording the SERS fingerprint at a defined area. An image map (Figure 8a) was then generated by selection of the Raman signal at 1078 cm^{-1}, corresponding to the ring stretch vibration mode of 4-MBA (peak labeled with arrow in Figure 8b), and overlaid in Figure 8a with the transmission light microscopy image of the cell culture. Red pixels corresponding to high intensity SERS signals (see scale bar), indicating the presence of 4-MBA-labeled nanoparticles within the cell areas while no nanoparticles were observed outside of the washed cells. In this experiment, higher signals would be expected for nanoparticles with a larger gold nanostar domain,[70,71] but even nanostars as small as 28 nm were found to provide a readable signal for SERS mapping.

Conclusions

Janus magneto-plasmonic JMNSs have been shown to be highly versatile and compact nanoparticles that integrate superparamagnetism and plasmonic responses at the NIR biological transparency window. Furthermore, their two chemically distinct surfaces allow easy functionalization. These

features render JMNSs excellent candidates for biomedical applications such as photo- and magneto-thermal therapies, or targeted and controlled drug delivery. Their use as contrast agents in multimodal imaging enables the use of complementary techniques to obtain maximum information. We demonstrated the use of JMNSs in several imaging techniques, such as MRI, CT, PA, optical imaging under bright and dark field illumination, TEM and SERS imaging. Compared with core-shell nanoparticles, the Janus morphology resulted highly beneficial in several aspects, offering high availability of the iron oxide surface, which consequently gives rise to high r_2 relaxivity values and Prussian blue staining ability. On the other hand, when compared with conventional Janus dumbbell-like nanoparticles, the nanostar morphology enables their use in photoacoustic and SERS imaging in the NIR biological window. We propose that their use could be easily translated to other techniques, such as NIR optical tomography, ultrasound, magnetophotoacoustic, or photothermal imaging, among others. Furthermore, their easy functionalization could also allow complementary imaging such as PET, SPECT, or fluorescent imaging. Finally, their Janus character could be further exploited in biomedical applications where an asymmetric positioning of functional groups may produce specific interactions with biological entities, in analogy to proteins.

Experimental

a. Synthesis

a.1 Chemicals

All chemicals were used as purchased without further purification: hydrogen tetrachloroaurate(III) trihydrate (99.99%, Alfa Aesar), oleylamine (80-90%, Acros Organics), 1-octadecene (90%, Aldrich), oleic acid (90%, Aldrich), iron(0) pentacarbonyl (99.99%, Aldrich), 1,2-hexadecanediol (90%, Aldrich), methoxypolyethylene glycol acetic acid (80%, Mn = 5000 g/mol), polyvinylpyrrolidone (Mn=10000, Aldrich) thiol-terminated PEG (Mn = 750 g/mol, Polymer Source), 4-mercaptobenzoic acid (90%, Aldrich), additional solvents were reagent grade from Aldrich.

a.2 Asymmetric dumbbells

-. 16 nm iron oxide

The synthesis of these heterodimers was performed as previously reported.[26] Briefly, for the 15 nm iron oxide part. A solution in 1-octadecane (40 mL) was prepared containing oleic acid (6 mmol, 1.90mL), oleylamine (6 mmol, 1.97mL) and 1,2-hexadecanediol (10 mmol, 2.58g) and stirred for 20 min at 120 ºC under N_2. $Fe(CO)_5$ (0.3 mL) was then injected and after 3 min a solution containing $HAuCl_4 \cdot 3H_2O$ (0.1 mmol) dissolved in a mixture of oleylamine (0.5 mL) and 1-octadecane (5 mL) was injected and heated up to 300 °C at approximately 1 °C/min. The solution was left to react for 45 min under magnetic stirring. After cooling down, the dispersion was exposed to air for 30 min to cause Fe oxidation.

-. 20 nm iron oxide

A solution in 1-octadecane (47 mL) was prepared containing oleic acid (6 mmol, 1.90mL), oleylamine (6 mmol, 1.97 mL) and 1,2-hexadecanediol (10 mmol, 2.58 g) and stirred for 15 min at 160 ºC under N_2. $Fe(CO)_5$ (2 mL) was then injected and after 3 min a solution containing $HAuCl_4 \cdot 3H_2O$ (40mg) dissolved in a mixture of oleylamine (0.5 mL) and 1-octadecane (3 mL) was injected and heated up to 310 °C at approximately 3 °C/min. The solution was left to react for 45 min, under mechanic stirring. After cooling down, the dispersion was exposed to air for 30 min to cause Fe oxidation.

-. Purification

To purify the nanoparticles, 50 mL of isopropanol was added and the solution centrifuged at 4500 g for 30 min. The nanoparticles were cleaned two more times after redispersion with hexane and aggregation with isopropanol. Finally oleylamine (100 µL) was added to store the nanoparticles for long periods of time in a hexane-chloroform solution.

a.3 Janus magnetic nanostars

The nanodumbbells were cleaned three times in ethanol and redispersed in chloroform to remove as much as oleylamine as possible. Finally they were redispersed in chloroform at a concentration of approximately 2 mg/mL. A small quantity of carboxyl terminated PEG was added to the solution (to have approximately 2mg/mL of polymer) and left for 1h. This step was performed to obtain a good dispersion when the seeds were added to the DMF gold solution.

A solution of $HAuCl_4 \cdot 3H_2O$ (2.184 mL, 50 mM) was added to a solution containing polyvinylpyrrolidone (PVP) (40 g, MW = 10 Kg/mol) dissolved in DMF (400 mL). The solution was left stirring to allow gold salt prereduction from Au^{3+} to Au^{+} as described elsewhere,[73] (this time was highly dependent on the PVP batch and needed to be adjusted by UV-vis, in this case it was 5 min). The dumbbell nanoparticle solution (at different volumes) was then quickly added and the reaction was left reacting for 1 h, showing a fast color change into blue. The nanoparticles were purified in 4 centrifugation cycles, redispersed the 2 times in ethanol and 2 times in water and at a relative centrifugation force of 2500-4000 g, depending on the nanoparticle size. The nanoparticles were finally redispersed in 40 mL of ultrapure water.

The volume of seeds was: JMNS.16.47 (0.25 mL); JMNS.16.43 (1 mL); JMNS.16.37 (2 mL); JMNS.16.28 (4 mL); JMNS.16.25 (8 mL); JMNS.16.19 (this was a scaled down reaction, 80 µL of seeds in 2 mL of DMF, 0.2 g of PVP, 10 µL of gold salt); JMNS.20.41 (0.5 mL) JMNS.20.36 (2 mL) JMNS.20.43 (4 mL).

a.4 MBA functionalization for SERS

Nanoparticles N0.16.28 were functionalized with 4-mercaptobenzoic acid (4-MBA), which acted as SERS tag, and with thiol terminated polyethylene glycol (PEG) to enhance colloidal stability. The nanoparticles were incubated overnight with an aqueous solution containing both ligands at a concentration of around ~50 ligands/nm^2 and a ratio 4-MBA:PEG 4:1 (1 mL of N0.16.28 [Au]= 1.95 mM, and 4.3 and 5.2 µg of MBA and PEG respectively). Diluted NaOH (0.2 M) was added drop-wise to 4-MBA (until it was completely dissolved) before adding it to the nanoparticle solution. The final nanoparticles were washed by two centrifugation cycles

in water and finally redissolve in 200 µL of milliQ water. The binding of 4-MBA to the nanoparticle surface was checked by measuring the SERS signal of the nanoparticle solution and identifying the MBA typical peaks.

b. Magnetic characterization

Hysteresis loops at room temperature were measured in a home-made Vibrating Sample Magnetometer (VSM) with a sensitivity of $5 \cdot 10^{-6}$ emu up to a maximum field of 18 kOe.

The measurements of magnetization versus temperature at 10 Oe were carried out in the temperature range of 5-300 K using a Quantum Design MPMS3 VSM-SQUID magnetometer with a sensitivity of 10^{-8} emu up to a maximum field of 7 T.

Using a Non-Interacting Super-Paramagnetic model to fit the obtained M(H) curves, an effective magnetic size of the particles was estimated. This approach neglects interparticle interactions that tend to reduce the initial susceptibility (slope of M(H) at low fields) and therefore the mean apparent size. Fitting of the magnetization versus temperature, ZFC/FC measurements, in the framework of the Non-Interacting model was also performed. The applied models and the fitting of the different graphs are described in the supporting info. For the fittings a saturation magnetization value of 400 emu/cm^3 was assumed.

c. ICP

The solution for ICP was prepared by adding aqua regia to a solution of nanoparticles, approximately at 15%. Dilutions of the sample were prepared and all of them were analyzed and quantified. An internal standard was carried out adding 100 µL of Yttrium at 500 ppb.

The analysis was performed by ICP-MS with a helium collision cell. The measured selected isotopes to perform the quantification were ^{57}Fe, ^{197}Au, at concentrations of 0.2-1000 µg/L. Table 1 shows the Au/Fe ratios measured by ICP for nanoparticles with 15 and 20 nm iron oxide respectively and different nanostar sizes.

d. TEM

TEM bright field images were acquired in a JEOL JEM-1400PLUS instrument operating at 120 kV, after nanoparticles were deposited on a carbon coated TEM grid. The nanoparticles were analyzed with the Image J software package. TEM images and final sizes are available in the supporting information and in Table 1.

High-resolution images and EDX mapping were obtained in a JEOL JEM-2100F UHR (80kV - 200 kV), equipped with STEM (BF & HAADF) and OXFORD INCA EDXS systems, and a TVIPS F216 CMOS camera (2k x 2k).

e. MRI

Proton relaxation times T_1 and T_2 were measured at 1.5 Tesla in a Bruker Minispec NMR spectrometer. Solutions of nanoparticles were prepared at 4-5 different concentrations (see SI) and were analyzed at 37 ºC using the methods described elsewhere.[74] Relaxivity values r_1 and r_2 were obtained from the slopes of the curves $1/T_1$ and $1/T_2$ vs. the concentration of Fe expressed in mM, respectively. The $1/T_{1,2}$ vs. concentration plots are represented in the supporting information. Imaging of phantoms was performed using a 7 T BioSpec 70/30USR (Brucker) in 200 µL solutions of ND.16.28 at different nanoparticle concentrations.

Table 1. Characteristic parameters of the different JMNS versions. TEM sizes, ICP elemental analysis, and magnetic relaxivities.

Sample	Average diameter (nm)	Au/Fe (mol/mol) by ICP	r_2 (s^{-1} mM^{-1})	r_1 (s^{-1} mM^{-1})
JMNS.16.47	46.9±8.2	29.1	176.3	5.49
JMNS.16.43	43.0±6.8	16.9	195.2	7.83
JMNS.16.37	36.7±4.9	9.0	210.8	9.43
JMNS.16.28	28.5±2.9	3.8	285.3	12.6
JMNS.16.25	25.0+-2.9	2.0	294.6	13.6
JMNS.16.19	19.4±3.2	0.24	-	-
JMNS.20.43	43.2±10.3	22.9	320.3	6.23
JMNS.20.41	41.6±5.9	4.0	381.4	8.79
JMNS.20.36	35.8±5	2.3	375.1	9.57

f. CT

Nanoparticles were diluted at several concentrations (see SI) and the coefficient of attenuation was calculated from the slope of attenuation vs. Au concentration (see supporting information).

CT images were acquired using the eXplore speCZT CT preclinical imaging system (GE Healthcare, Milwaukee, USA). The acquisition protocols were implemented by the vendor and could not be modified. The protocols employed in terms of X-ray tube voltage and current were: 1) 70 kV, 32 mA; 2) 80 kV, 32 mA; and 3) 100kV, 50mA. For protocol 1 and 2, the acquisition consisted of 220 views were acquired in 0.88° increments around the phantom with 16 ms exposure per view. In case of protocol 3, 360 views were acquired in 1° increments with 20 ms exposure per view. The CT images were reconstructed using a cone beam filtered back-projection Feldkamp algorithm into 437 × 437 × 523 array with a voxel size of 0.2 × 0.2 × 0.2 mm for data collected with protocol 1 and 2, and into 875 x 875 x 1047 array with voxel size of 0.1 x 0.1 x 0.1 mm for data collected with protocol 3.

g. Photoacoustic imaging (PA)

The PA measurements were acquired using the Vevo LAZR Photoacoustic Imaging System (FUJIFILM VisualSonics Inc., Toronto). An ultrasound transducer with an operating frequency range of 13−24 MHz was used to receive photoacoustic signals generated from the nanoparticles. A tunable Nd:YAG laser excitation system was used to induce near infrared (NIR) laser in the wavelength range of 680–970 nm. Vevo® LAB software (FUJIFILM VisualSonics Inc., Toronto) was used to reconstruct the ultrasound and photoacoustic images from the acoustic signals. The phantoms were prepared mixing the nanoparticles in aqueous dispersion with a 1.5% agarose water-based solution at different concentrations of Au, and then transferred into 20-50 µL wells embedded in a solidified 1.5% agarose gel.

h. Cell cultures imaging

h.1 Sample preparation and optical imaging

A concentrated solution of 4 MBA-functionalized nanoparticles N0.16.28 [see synthesis, [Au]~1mM] was diluted in cell media (DMEM containing fetal bovine serum and penicillin-streptomycin to final concentrations of 10 % and 1 % respectively) to reach a concentration of 50 µM, prior to the incubation experiment.

Adenocarcinomic human alveolar basal epithelial cells (A549) cells were grown on glass slides in a 24-well plate and incubated with the NP solution (25 µL NP/well) overnight. Samples were washed with PBS to remove non-endocytosed NPs and fixed in 4% formaldehyde. Samples were stained with a 1:1 solution of 4% w/v Prussian yellow and 4% v/v HCl for 30 minutes at room temperature. Samples were thoroughly washed with water followed by neutral red counter stain (2 mg/mL, 20 seconds). Samples were again thoroughly washed and then mounted on glass cover slips. The samples were imaged with a Nikon microscope using a dry 60x objective and dry condenser moving to high (bright field) or low (dark field) positions. Exposition time was set at 0.08 s and neutral density filters used.

h.2 TEM cell imaging

A549 cells were incubated overnight with 4-MBA functionalized nanoparticles N0.16.28 at a final concentration of 50 µM. Cells were trypsinized and fixed in 0.1 M Sorensens buffer with 2% formaldehyde and 2.5% glutaraldehyde. Cells were transferred to a 2% molten agar solution and once hardened, small 1 mm^3 pieces were cut and pre-stained with a 1% solution of Osmodium tetraoxide, OsO_4, in Sorensens buffer. After 1hr staining at 4 °C, samples were washed and an ethanol dehydration series followed by two 100% acetone washes was carried out. Samples were embedded in Spurrs resin (EMS) and cured overnight at 60 ºC before 100 nm slices were cut using a Leica Ultramicrotome. Slices were transferred to carbon-coated grids and imaged with a JEOL JEM-1400PLUS TEM operating at 120 kV.

i. SERS mapping

SERS mappings were performed by means of a confocal Raman microscope (Renishaw inVia) equipped with a 1024 x 512 CCD Peltier- cooled detector using the 785 nm excitation laser with maximal output of 270 mW combined with a 1200 grooves/mm diffraction grating and a 40x water immersion objective (numerical aperture of 0.8).

A549 cells were grown on a quartz glass slide and incubated overnight 4-MBA functionalized JMNS.16.28 nanoparticles, prepared as described above, followed by washing with warmed media to remove non-uptaken NPs. The SERS measurement was performed using living cells within a home-build dish (diameter 9 mm, volume of 250 µL) having a Quartz glass slide support. SERS maps were recorded on a 1x1 µm grid for 1s per pixel at a laser power of 16 mW (measured at surface in air), after signal intensity optimization of the vertical z position.

Acknowledgements

This work has been funded by the European Research Council (ERC Advanced Grant #267867, Plasmaquo) and

MINECO (Grant MAT2013-46101-R). SGIker technical and human support (UPV/EHU, MINECO, GV/EJ, FEDER Y FSE) for the ICP measurements, Dr. Sergio Moya is thanked for providing A549 cells, and Luis Yate, Marco Möller, Iñaki Orue-Goikuria and Daniel Padró are thanked for their help with experimental techniques.

References

1. D.-E. Lee, H. Koo, I.-C. Sun, J. H. Ryu, K. Kim and I. C. Kwon, *Chem. Soc. Rev.*, 2012, **41**, 2656-2672.
2. C. M. C. Tempany, J. Jayender, T. Kapur, R. Bueno, A. Golby, N. Agar and F. A. Jolesz, *Cancer*, 2015, **121**, 817-827.
3. S. Y. Lee, S. I. Jeon, S. Jung, I. J. Chung and C.-H. Ahn, *Adv. Drug Del. Rev.*, 2014, **76**, 60-78.
4. J. Rieffel, U. Chitgupi and J. F. Lovell, *Small*, 2015, **11**, 4445-4461.
5. T.-H. Shin, Y. Choi, S. Kim and J. Cheon, *Chem. Soc. Rev.*, 2015, **44**, 4501-4516.
6. J. Key and J. F. Leary, *Int. J. Nanomedicine*, 2014, **9**, 711-726.
7. N. Lee, D. Yoo, D. Ling, M. H. Cho, T. Hyeon and J. Cheon, *Chem. Rev.*, 2015, **115**, 10637-10689.
8. S. Laurent, D. Forge, M. Port, A. Roch, C. Robic, L. Vander Elst and R. N. Muller, *Chem. Rev.*, 2008, **108**, 2064-2110.
9. A. Espinosa, R. Di Corato, J. Kolosnjaj-Tabi, P. Flaud, T. Pellegrino and C. Wilhelm, *ACS Nano*, 2016, **10**, 2436-2446.
10. E. C. Dreaden, A. M. Alkilany, X. Huang, C. J. Murphy and M. A. El-Sayed, *Chem. Soc. Rev.*, 2012, **41**, 2740-2779.
11. E. Boisselier and D. Astruc, *Chem. Soc. Rev.*, 2009, **38**, 1759-1782.
12. X. Zhao, L. Xu, M. Sun, W. Ma, X. Wu, H. Kuang, L. Wang and C. Xu, *Small*, 2016, **12**, 4662-4668.
13. M. Sun, L. Xu, W. Ma, X. Wu, H. Kuang, L. Wang and C. Xu, *Adv. Mater.*, 2016, **28**, 898-904.
14. S. Li, L. Xu, M. Sun, X. Wu, L. Liu, H. Kuang and C. Xu, *Adv. Mater.*, 2017, **29**,1606086.
15. H. Zhou, F. Zou, K. Koh and J. Lee, *J. Biomed. Nanotechnol.*, 2014, **10**, 2921-2949.
16. C. S. Levin, C. Hofmann, T. A. Ali, A. T. Kelly, E. Morosan, P. Nordlander, K. H. Whitmire and N. J. Halas, *ACS Nano*, 2009, **3**, 1379-1388.
17. H. M. Song, Q. S. Wei, Q. K. Ong and A. Wei, *ACS Nano*, 2010, **4**, 5163-5173.
18. Z. Xu, Y. Hou and S. Sun, *J. Am. Chem. Soc.*, 2007, **129**, 8698-8699.
19. L. Wang, J. Bai, Y. Li and Y. Huang, *Angew. Chem. Int. Ed.*, 2008, **47**, 2439-2442.
20. J. Li, Y. Hu, J. Yang, P. Wei, W. Sun, M. Shen, G. Zhang and X. Shi, *Biomaterials*, 2015, **38**, 10-21.
21. H. Zhou, J.-P. Kim, J. H. Bahng, N. A. Kotov and J. Lee, *Adv. Funct. Mater.*, 2013, **24**, 1439-1448.
22. Y. Jin, C. Jia, S.-W. Huang, M. O'Donnell and X. Gao, *Nat. Commun.*, 2010, **1**, 1-8.
23. M. Carril, I. Fernández, J. Rodríguez, I. García and S. Penadés, *Part. Part. Syst. Charact.*, 2013, **31**, 81-87.
24. L. Lou, K. Yu, Z. Zhang, R. Huang, Y. Wang and Z. Zhu, *Appl. Surf. Sci.*, 2012.
25. J. A. Hachtel, S. Yu, A. R. Lupini, S. T. Pantelides, M. Gich, A. Laromaine and A. Roig, *Faraday Discuss.*, 2016, **191**, 215-227.
26. H. Yu, M. Chen, P. M. Rice, S. X. Wang, R. L. White and S. H. Sun, *Nano Lett.*, 2005, **5**, 379-382.
27. Y. Lee, M. A. Garcia, N. A. Frey Huls and S. Sun, *Angew. Chem. Int. Ed.*, 2010, **49**, 1271-1274.
28. M. Wang, C. Wang, K. L. Young, L. Hao, M. Medved, T. Rajh, H. C. Fry, L. Zhu, G. S. Karczmar, C. Watson, J. S. Jiang, N. M. Markovic and V. R. Stamenkovic, *Chem. Mater.*, 2012, **24**, 2423-2425.
29. P.-J. Chen, Y.-D. Kang, C.-H. Lin, S.-Y. Chen, C.-H. Hsieh, Y.-Y. Chen, C.-W. Chiang, W. Lee, C.-Y. Hsu, L.-D. Liao, C.-T. Fan, M.-L. Li and W.-C. Shyu, *Adv. Mater.*, 2015, **27**, 6488-6495.
30. A. La Porta, A. Sánchez-Iglesias, T. Altantzis, S. Bals, M. Grzelczak and L. M. Liz-Marzán, *Nanoscale*, 2015, **7**, 10377-10381.
31. M. A. Fernandez-Rodriguez, M. Á. Rodríguez-Valverde, M. A. Cabrerizo-Vilchez and R. Hidalgo-Alvarez, *Adv. Colloid Interface Sci.*, 2016, **233 IS -**, 240-254.
32. A. Kumar, B. J. Park, F. Tu and D. Lee, *Soft Matter*, 2013, **9**, 6604.
33. J. Reguera, H. Kim and F. Stellacci, *Chimia*, 2013, **67**, 811-818.
34. H. Kim, R. P. Carney, J. Reguera, Q. K. Ong, X. Liu and F. Stellacci, *Adv. Mater.*, 2012, **24**, 3857-3863.
35. D. Rodríguez-Fernández and L. M. Liz-Marzán, *Part. Part. Syst. Charact.*, 2013, **30**, 46-60.
36. A. Walther and A. H. E. Müller, *Chem. Rev.*, 2013, **113**, 5194-5261.
37. P. R. Leroueil, S. Hong, A. Mecke, J. R. J. Baker, B. G. Orr and M. M. B. Holl, *Acc. Chem. Res.*, 2007, **40**, 335-342.
38. H.-M. Ding and Y.-Q. Ma, *Nanoscale*, 2012, **4**, 1116-1122.
39. Q.-S. Xia, H.-M. Ding and Y.-Q. Ma, *Nanoscale*, 2017, DOI: 10.1039/C7NR01020F.
40. R. Weissleder, *Nat. Biotechnol.*, 2001, **19**, 316-317.
41. A. M. Smith, M. C. Mancini and S. Nie, *Nat. Nanotechnol.*, 2009, **4**, 710-711.

42. J. Reguera, D. Jiménez de Aberasturi, N. Winckelmans, J. Langer, S. Bals and L. M. Liz-Marzán, *Farad. Discuss.*, 2016, **191**, 47-59.
43. L. Wu, A. Mendoza-Garcia, Q. Li and S. Sun, *Chem. Rev.*, 2016, **116**, 10473-10512.
44. R. Hao, R. Xing, Z. Xu, Y. Hou, S. Gao and S. Sun, *Adv. Mater.*, 2010, **22**, 2729-2742.
45. C. Xu, J. Xie, D. Ho, C. Wang, N. Kohler, E. G. Walsh, J. R. Morgan, Y. E. Chin and S. Sun, *Angew. Chem. Int. Ed.*, 2008, **47**, 173-176.
46. F. Hao, C. L. Nehl, J. H. Hafner and P. Nordlander, *Nano Lett.*, 2007, **7**, 729-732.
47. I. Schick, D. Gehrig, M. Montigny, B. Balke, M. Panthöfer, A. Henkel, F. Laquai and W. Tremel, *Chem. Mater.*, 2015, **27**, 4877-4884.
48. L. Rodríguez-Lorenzo, J. M. Romo-Herrera, J. Pérez-Juste, R. A. Alvarez-Puebla and L. M. Liz-Marzán, *J. Mater. Chem.*, 2011, **21**, 11544-11549.
49. A. Kedia and P. S. Kumar, *J. Mater. Chem. C*, 2013, **1**, 4540-4549.
50. N. Lee and T. Hyeon, *Chem. Soc. Rev.*, 2012, **41**, 2575-2589.
51. H. Kloust, R. Zierold, J.-P. Merkl, C. Schmidtke, A. Feld, E. Pöselt, A. Kornowski, K. Nielsch and H. Weller, *Chem. Mater.*, 2015, **27**, 4914-4917.
52. L. E. W. LaConte, N. Nitin, O. Zurkiya, D. Caruntu, C. J. O'Connor, X. Hu and G. Bao, *J. Magn. Reson. Imaging*, 2007, **26**, 1634-1641.
53. D. Pouliquen, H. Perroud, F. Calza, P. Jallet and J. J. Le Jeune, *Magn. Reson. Med.*, 1992, **24**, 75-84.
54. S. Tong, S. Hou, Z. Zheng, J. Zhou and G. Bao, *Nano Lett.*, 2010, **10**, 4607-4613.
55. L. E. Cole, R. D. Ross, J. M. Tilley, T. Vargo-Gogola and R. K. Roeder, *Nanomedicine*, 2015, **10**, 321-341.
56. R. D. Ross, L. E. Cole, J. M. R. Tilley and R. K. Roeder, *Chem. Mater.*, 2014, **26**, 1187-1194.
57. R. Popovtzer, A. Agrawal, N. A. Kotov, A. Popovtzer, J. Balter, T. E. Carey and R. Kopelman, *Nano Lett.*, 2008, **8**, 4593-4596.
58. D. Wu, L. Huang, M. S. Jiang and H. Jiang, *Int. J. Mol. Sci.*, 2014, **15**, 23616-23639.
59. K. Wilson, K. Homan and S. Emelianov, *Nat. Commun.*, 2012, **3**, 618.
60. Q. Chen, J. Wen, H. Li, Y. Xu, F. Liu and S. Sun, *Biomaterials*, 2016, **106**, 144-166.
61. L. Xi, S. R. Grobmyer, G. Zhou, W. Qian, L. Yang and H. Jiang, *J Biophotonics*, 2014, **7**, 401-409.
62. A. Espinosa, A. K. A. Silva, A. Sánchez-Iglesias, M. Grzelczak, C. Péchoux, K. Desboeufs, L. M. Liz-Marzán and C. Wilhelm, *Adv. Healthc. Mater.*, 2016, **5**, 1040-1048.
63. S. Liang, C. Li, C. Zhang, Y. Chen, L. Xu, C. Bao, X. Wang, G. Liu, F. Zhang and D. Cui, *Theranostics*, 2015, **5**, 970-984.
64. X. Huang and M. A. El-Sayed, *J. Adv. Res.*, 2010, **1**, 13-28.
65. X. Huang, I. H. El-Sayed, W. Qian and M. A. El-Sayed, *J. Am. Chem. Soc.*, 2006, **128**, 2115-2120.
66. J. Yguerabide and E. E. Yguerabide, *Anal. Biochem.*, 1998, **262**, 137-156.
67. A.-I. Henry, B. Sharma, M. F. Cardinal, D. Kurouski and R. P. Van Duyne, *Anal. Chem.*, 2016, **88**, 6638-6647.
68. Y. Wang, B. Yan and L. Chen, *Chem. Rev.*, 2013, **113**, 1391-1428.
69. S. E. Bohndiek, A. Wagadarikar, C. L. Zavaleta, D. Van de Sompel, E. Garai, J. V. Jokerst, S. Yazdanfar and S. S. Gambhir, *Proc. Natl. Acad. Sci.*, 2013, **110**, 12408-12413.
70. J. Reguera, J. Langer, D. Jiménez de Aberasturi and L. M. Liz-Marzan, *Chem. Soc. Rev.*, 2017, DOI: 10.1039/c7cs00158d.
71. S. Schlücker, *Angew. Chem. Int. Ed.*, 2014, **53**, 4756-4795.
72. A. Guerrero-Martínez, S. Barbosa, I. Pastoriza-Santos and L. M. Liz-Marzán, *Curr. Opin. Colloid Interface Sci.*, 2011, **16**, 118-127.
73. S. Barbosa, A. Agrawal, L. Rodríguez-Lorenzo, I. Pastoriza-Santos, R. A. Alvarez-Puebla, A. Kornowski, H. Weller and L. M. Liz-Marzán, *Langmuir*, 2010, **26**, 14943-14950.
74. C. Henoumont, S. Laurent and L. Vander Elst, *Contrast Media Mol. Imaging*, 2009, **4**, 312-321.

TOC graphical abstract:

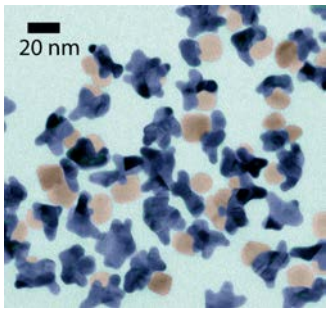

Janus Au-Fe_3O_4 star-sphere nanoparticles show their high versatility as contrast agents in multimodal imaging.

Janus plasmonic-magnetic gold-iron oxide nanoparticles as contrast agents for multimodal imaging

Javier Reguera,*[a,b,c] Dorleta Jiménez de Aberasturi,[a,b] Malou Henriksen-Lacey,[a,b] Judith Langer,[a,b] Ana Espinosa,[d] Boguslaw Szczupak,[a] Claire Wilhelm,[d] Luis M. Liz-Marzán[a,b,c]

[a] CIC biomaGUNE, Paseo de Miramón 182, 20014 Donostia-San Sebastián, Spain
[b] Biomedical Research Networking Center in Bioengineering Biomaterials and Nanomedicine, Ciber-BBN, 20014 Donostia-San Sebastián, Spain
[c] Ikerbasque, Basque Foundation for Science, 48013 Bilbao, Spain
[d] Laboratoire Matière et Systèmes Complexes, UMR 7057, CNRS and University Paris Diderot, 75205 Paris Cedex 13, France

1 TEM characterization

1.1 Asymmetric dumbbell nanoparticles

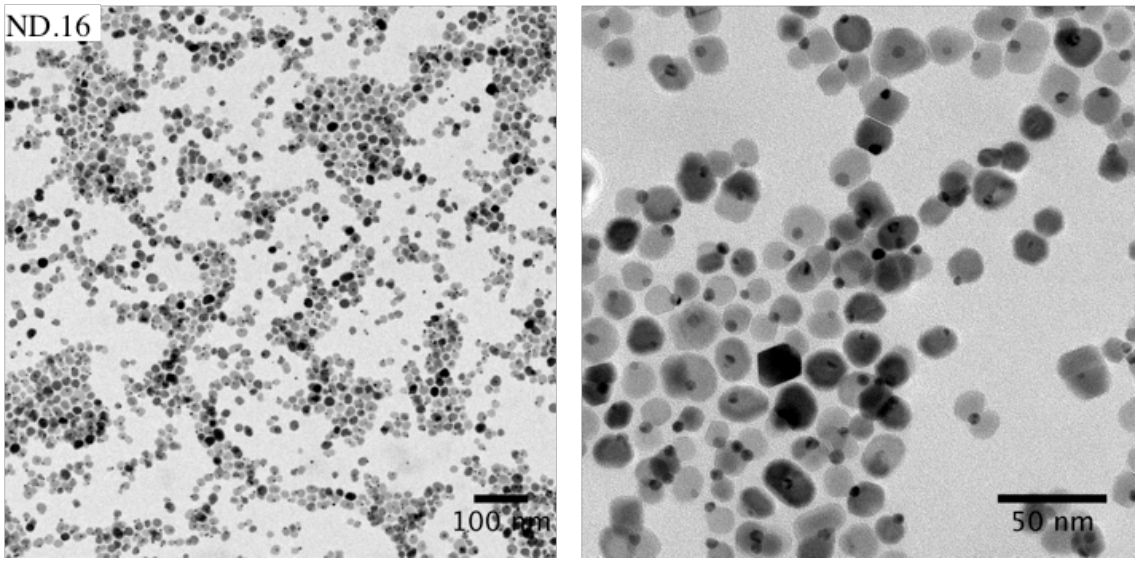

Figure S1: TEM images of nanodumbbells with 16 nm iron oxide cores.

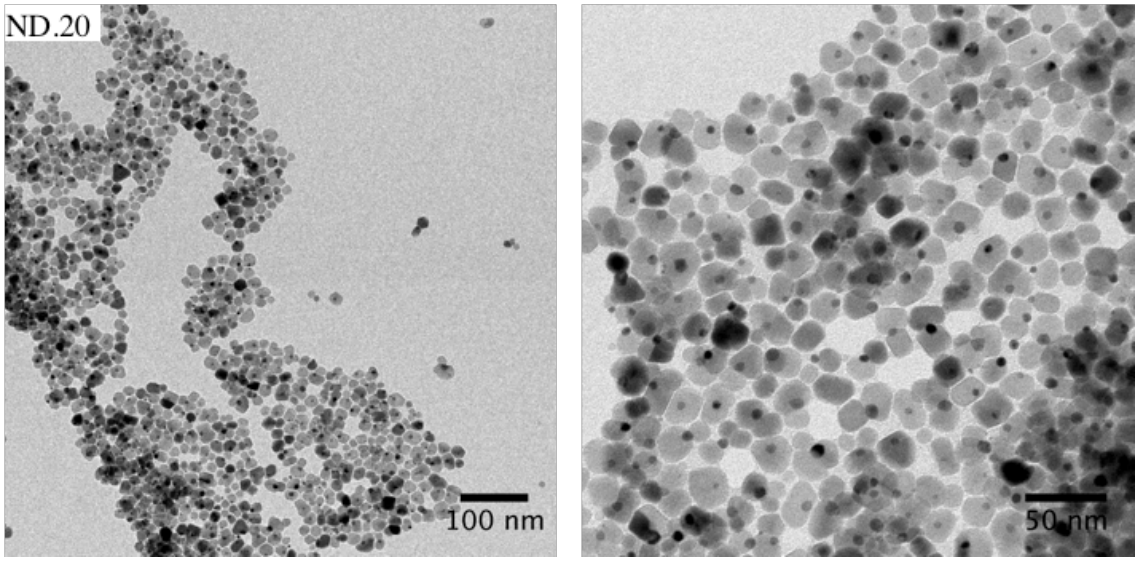

Figure S2: TEM images of nanodumbbells with 20 nm iron oxide cores.

1.2 Janus magnetoplasmonic nanostars (JMNSs)

- JMNSs with 16 nm iron oxide parts

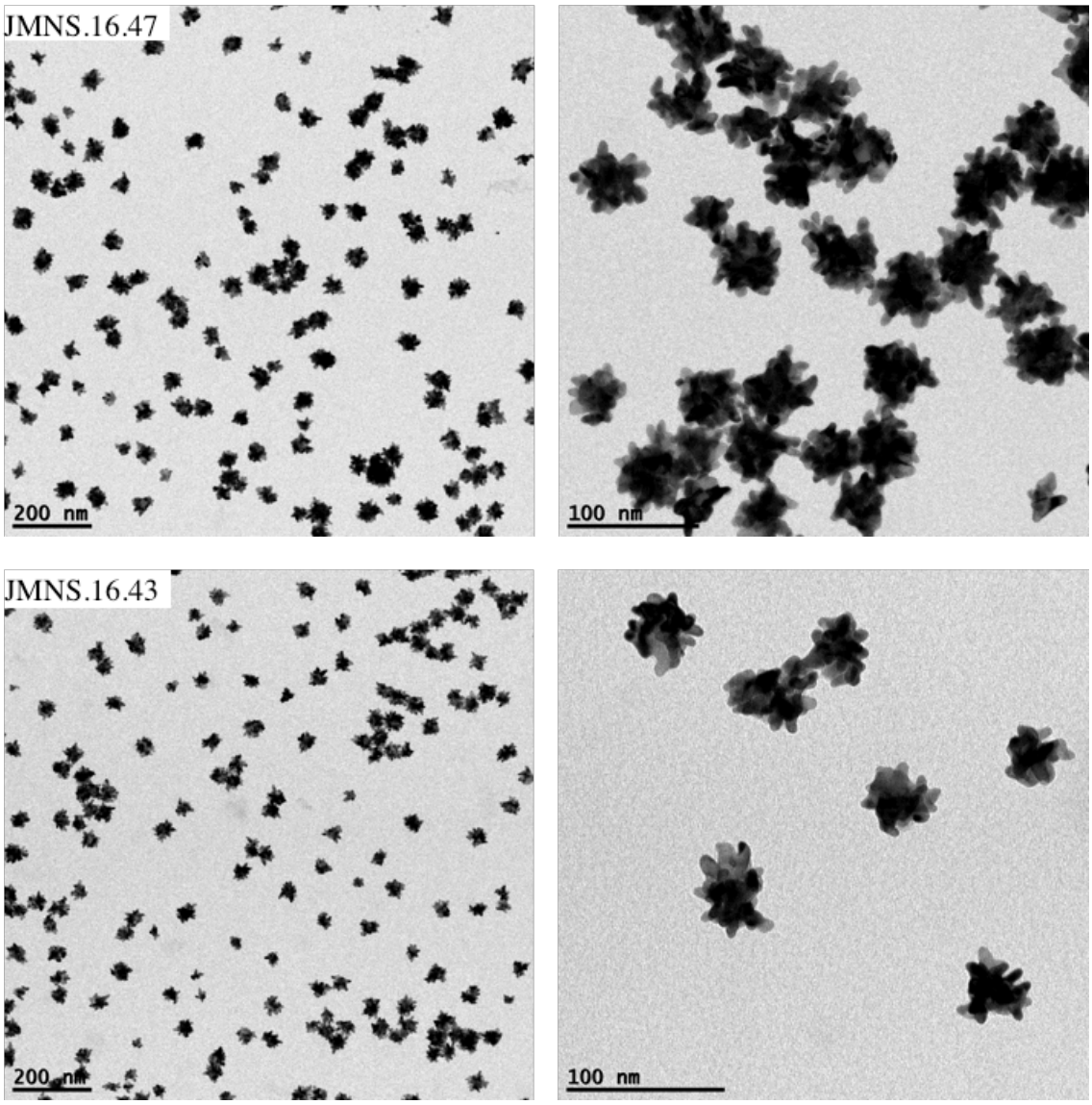

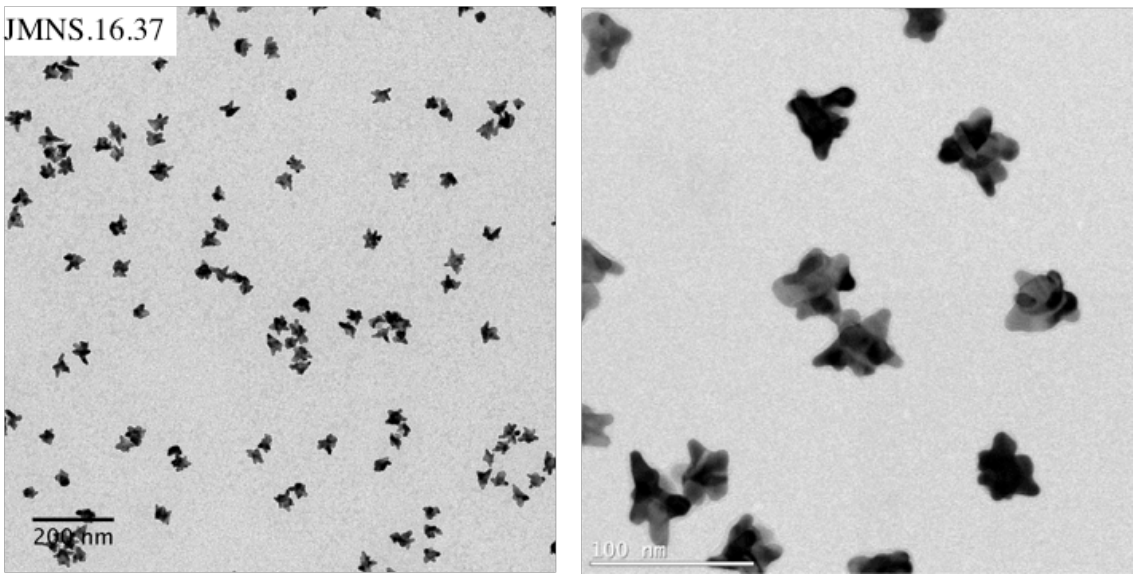
JMNS.16.37
200 nm
100 nm

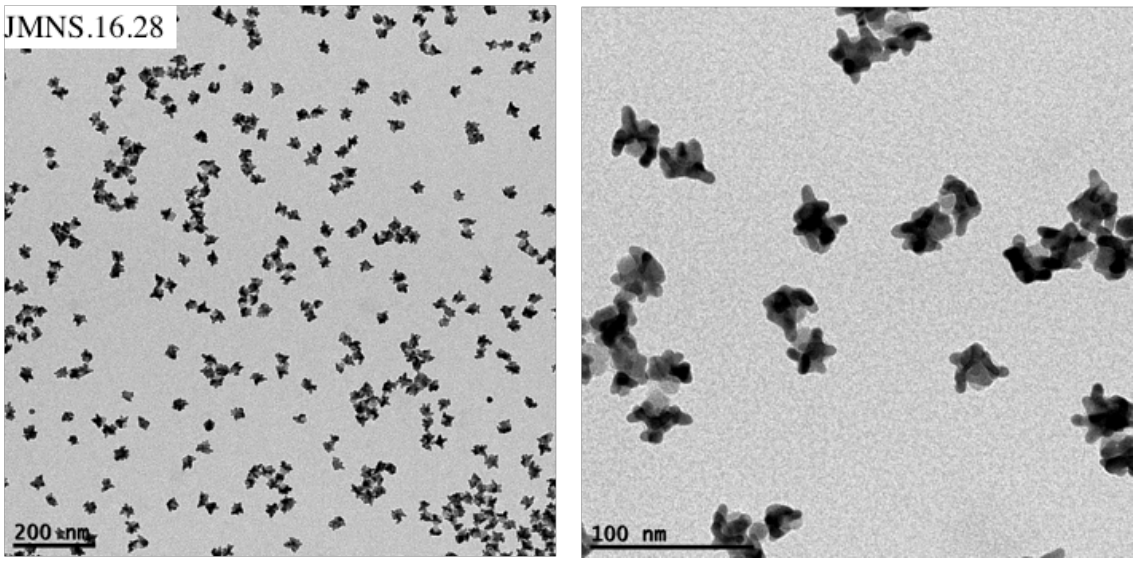
JMNS.16.28
200 nm
100 nm

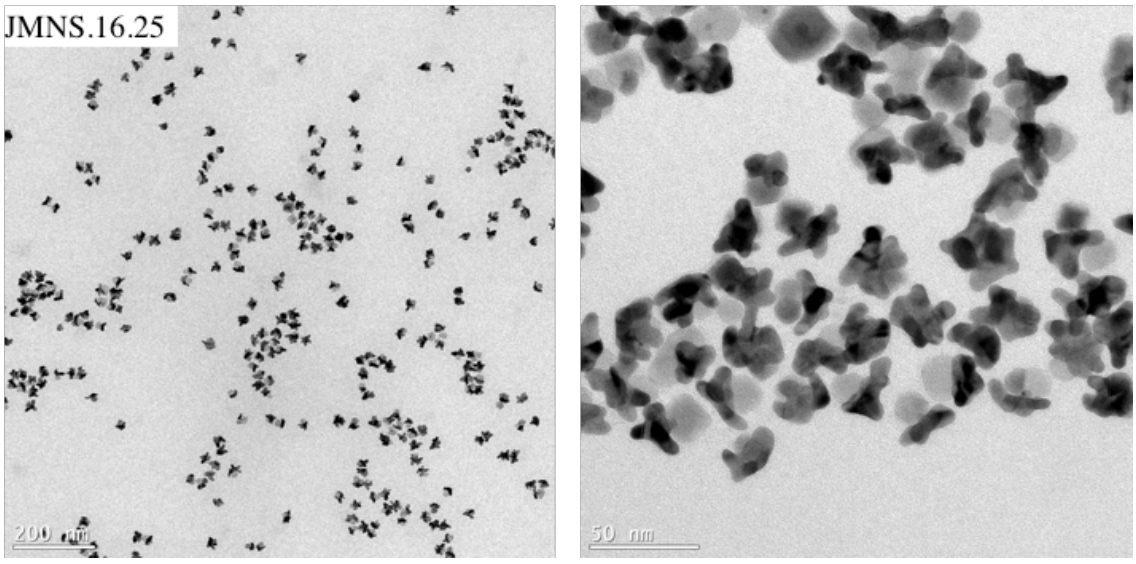
JMNS.16.25
200 nm
50 nm

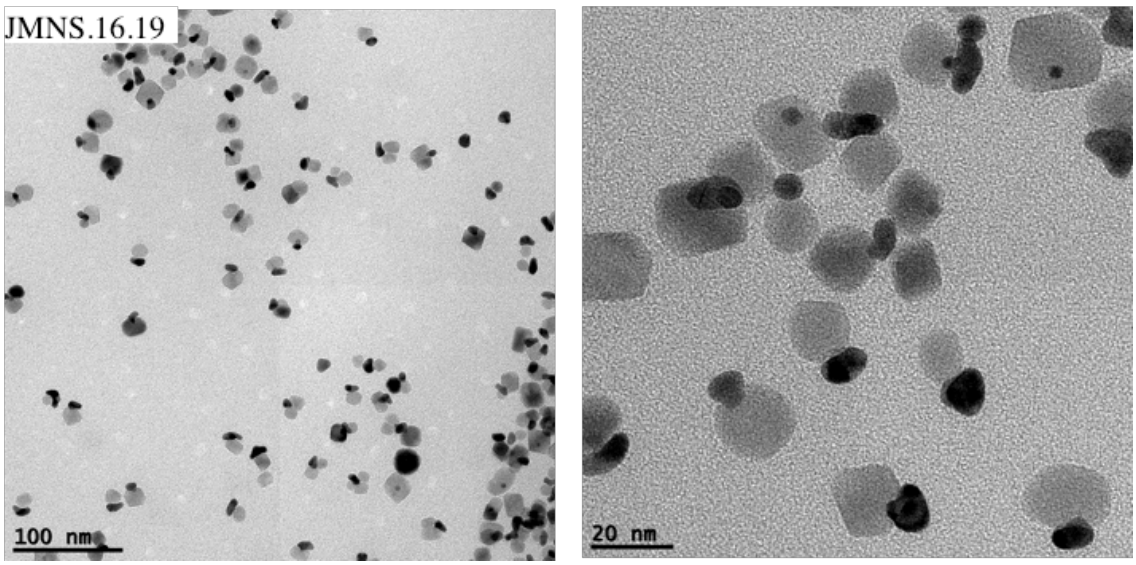

Figure S3: TEM images of JMNSs with 16 nm iron oxide parts.

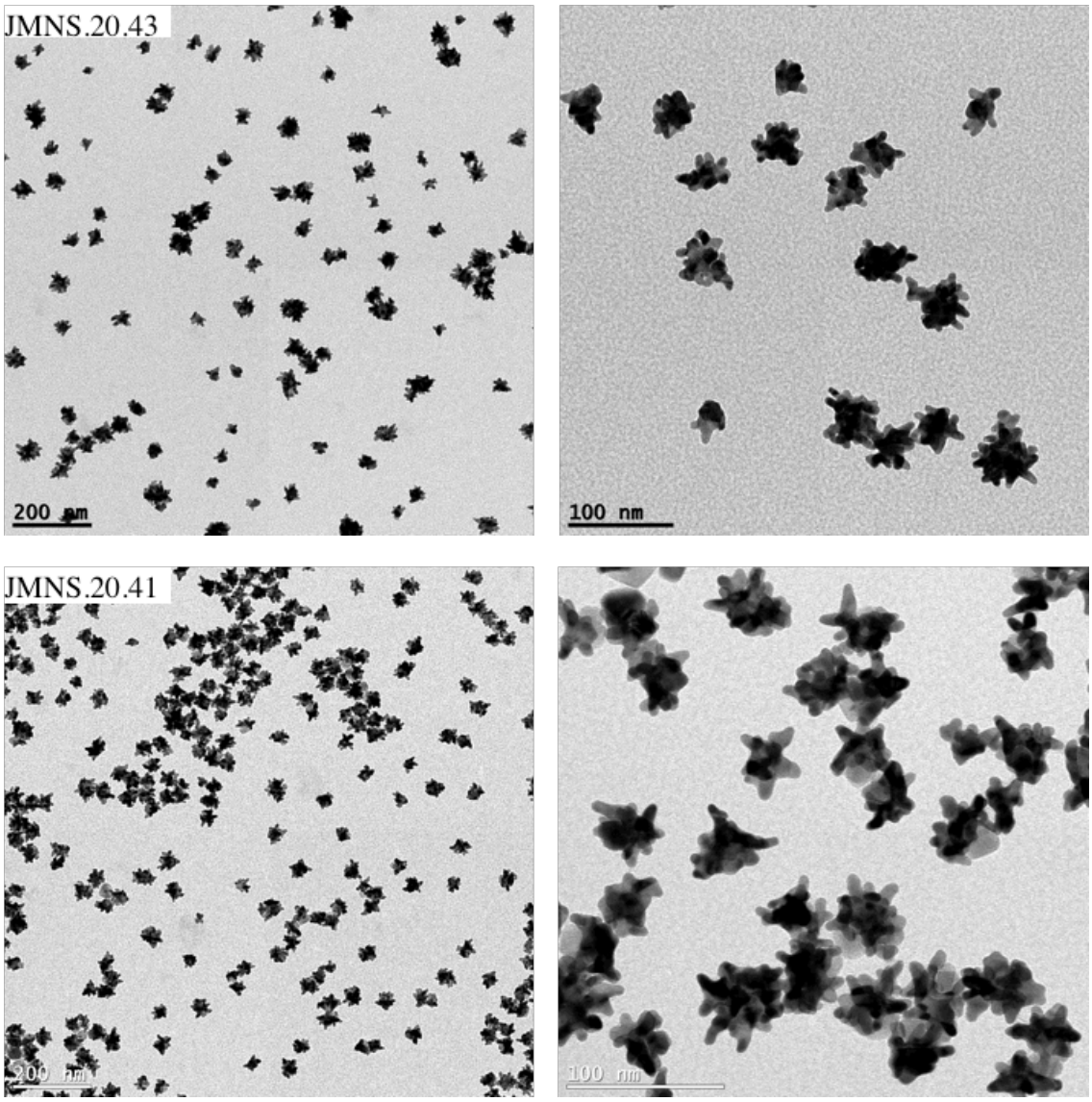

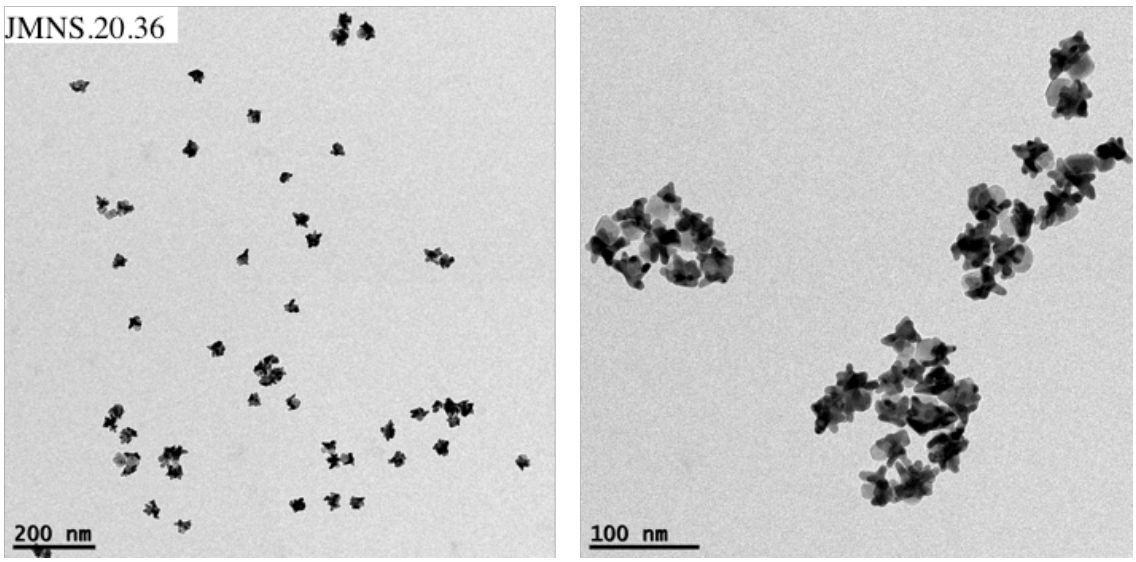

Figure S4: TEM images of JMNSs with 20 nm iron oxide parts.

2 Nanoparticle sizes

To calculate the size of the particles TEM was used. Several images per nanoparticle type were analyzed with the use of the software package Image J. The images were analyzed based on the gray scale contrast, making use of the threshold tools and particle analysis.

For the asymmetric nanodumbbells the gold part was first measured using its higher contrast (darker), and the iron oxide was them measured by removing the gold part and selecting the iron oxide based on grey scale levels. Manual measurements were performed where the grey scale did not offer a good contrast. The sizes of gold and iron oxide were calculated from the areas assuming a spherical shape (equivalent average diameter).

Table S1: Average diameter, measured by TEM, of the asymmetric nanodumbbells used as seeds in the JMNS synthesis.

	Iron oxide diameter (nm)	Gold diameter (nm)
ND.16	16.2± 2.8	5.3± 0.8
ND.20	20.5± 4.0	5.7± 1.2

For the JMNSs, only the total size was measured. Two different values were acquired: an equivalent average diameter, considering the area and assuming an equivalent spherical shape, and the Feret's maximum diameter that corresponds to the maximum tip to tip distance of the 2D projected nanostars. Error bars correspond to ± the standard deviation after the measurement of a minimum of 100 nanoparticles.

Average sizes are shown in the table and represented in the next graphs.

Table S2: Average diameter measured by TEM of the JMNSs. Equivalent diameter (assuming spherical nanoparticles) and Feret's (equivalent to a maximum tip to tip distance of the TEM image)

Sample	$D_{equivalent}$ (nm)	D_{Feret} (nm)
JMNS.16.47	46.9±8.2	59.8±10.5
JMNS.16.43	43.0±6.8	55.3±9.2
JMNS.16.37	36.7±4.9	50.6±8.2
JMNS.16.28	28.5±2.9	37.5±4.5
JMNS.16.25	25.0±2.9	31.9±4.5
JMNS.16.19	19.4±3.2	24.3±4.2
JMNS.20.43	43.2±10.3	56.2±13.3
JMNS.20.41	41.4±5.9	54.4±7.6
JMNS.20.36	35.8±5.0	45.9±7.3

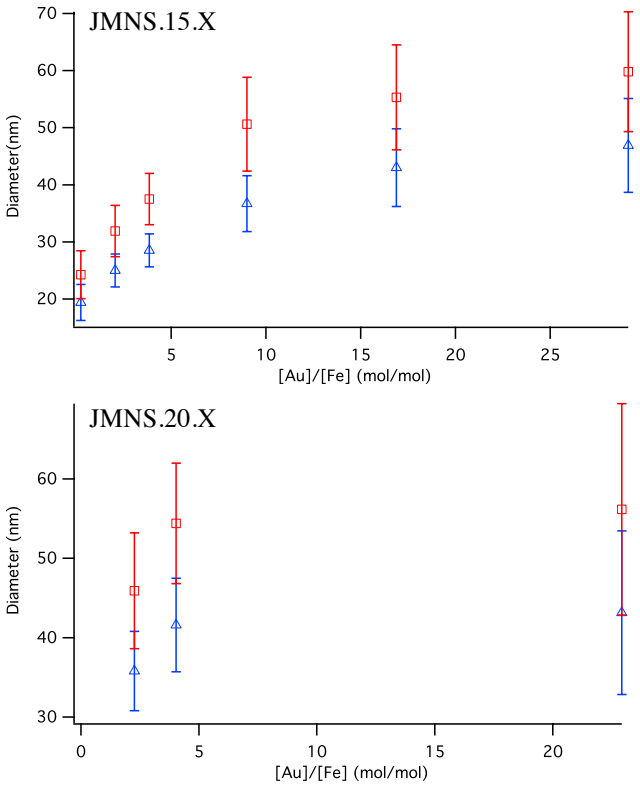

Figure S5: JMNS diameters, corresponding to nanoparticles with 16 nm and 20 nm iron oxide part, as a function of the gold to iron ratio used in the synthesis ($D_{equivalent}$ in red, D_{Feret} in red).

3 X-ray photoelectron spectroscopy (XPS)

XPS measurements were performed in a SPECS Sage HR 100 spectrometer with a non-monochromatic X-ray source (Aluminum Kα line of 1486.6 eV energy and 300 W), placed perpendicular to the analyzer axis and calibrated using the $3d_{5/2}$ line of

Ag with a full width at half maximum (FWHM) of 1.1 eV. The selected resolution for the spectra was 10 eV of pass energy and 0.15 eV/step. All measurements were made in an ultra high vacuum (UHV) chamber at a pressure around 5·10-8 mbar. The data was fitted using asymmetric and Gaussian-Lorentzian functions (after a Shirley background correction), where the FWHM of all the peaks were constrained while the peak positions and areas were set free.

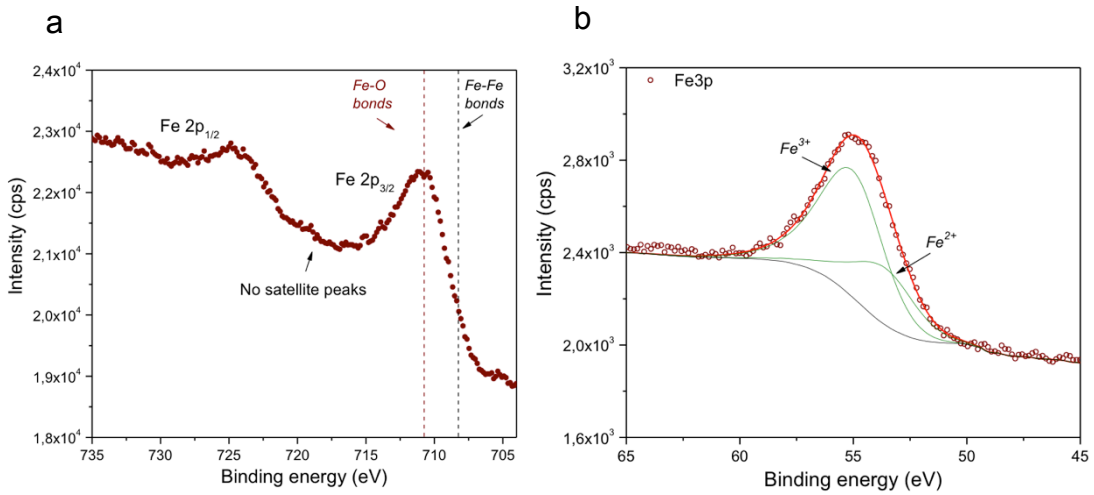

Figure S6: XPS spectra of ND.20 sample. **a**) Fe 2p spectrum. The absence of satellite or shake-up peaks indicates that the sample is mainly Fe_3O_4. Both FeO and Fe_2O_3 materials can be easily identified since they present satellite peaks at around 716 and 730, and 719 and 733 eV, respectively.[1,2] **b**) Fe 3p fitted spectrum. The Fe^{3+}/Fe^{2+} theoretical ratio for pure Fe_3O_4 is 2/1. The Fe^{3+}/Fe^{2+} ratio for the sample is around 2.2, which is in agreement with the shape of the Fe 2p spectrum.

4 Fitting of magnetic plots

The magnetic plots were analyzed by comparing the experimental results to several standard models.[3] Below is the detailed description of the Langevin and non-interacting models used to fit the experimental results, and the plots after fitting the models

4.1 Non-interacting Super-paramagnetic model: fit of M(H) measurements

The standard Langevin approach to the superparamagnetism (ideal SPM model) provides quantitative information about the size of the particles.[4]

The magnetization M of a magnetic nanoparticle system as a function of external field H and temperature T is defined as:

$$M = \frac{NM_o v}{V}(\coth x - 1/x) = M_s L(x) \quad x = M_o v \mu_o H / K_B T, \tag{1}$$

where N is the number of nanoparticles, v volume of a nanoparticle, V volume of the system, M_o bulk saturation magnetization, and Lx the Langevin function.[5,6]

In the Langevin model the nanoparticle sizes are assumed to be Gauss distributed around the mean hydrodynamic diameter D_h, and hence, the total magnetization of the system is not just Nv, but an integral over the measured size distribution:

$$\int_0^{max} L\left(\frac{M_o v \mu_o H}{K_B T}\right)$$

$$M = M_s \int_0^{max} L\left(\frac{M_o v \mu_o H}{K_B T}\right) f(D) dD \tag{2}$$

The magnetization of saturation, $[M_s] = A \cdot m^2$ (kg), is considered as a variable independent of the nanoparticles or domain magnetization, $[M] = kA$ (m^3) and both variables are related by the inorganic content of the sample and density. Often, domain magnetization initially M is fixed to the theoretical expected value, and with the fit a value for the mean size and polydispersity of the magnetic core is provided. Thus, the fit of these measurements at room temperature provides the calculation of the mean size and the standard deviation of the magnetic nanoparticles.

4.2 Determination of Anisotropy Constant

- Fit of ZFC/FC measurements

A non-interacting model was used to fit the obtained experimental measurements.[7] The population of magnetic nanoparticles (given by a size distribution fD) is divided in two groups at each temperature, depending on their nanoparticle size: the fraction in an ideal superparamagnetic state that corresponds to nanoparticles below a certain critical volume and those, above such limit, whose super spin remains blocked:

$$M_{ZFC}(T) = \int_0^{V_c(K_{eff},T)} M_s L\left(\frac{MVH}{k_B T}\right) f(V)dV + \int_{V_c(K_{eff},T)}^{\infty} M_s \frac{MH}{3K_{u,c}} f(V)dV \qquad (3)$$

In the first term, the low energy barrier approximation is used, where the energy barrier (defined as $K_{\text{eff}} V$, being V the nanoparticle volume) is much smaller than the thermal energy ($k_{\text{B}} T$ where k_{B} is the Boltzmann Constant), and thus can be omitted. As a consequence, the response of the magnetization to changes of magnetic field or temperature (H or T) follows a Langevin function, where M is the particle magnetization (A/m in S.I.) and M_{s} is the experimental saturation magnetization (including non-magnetic mass contribution, in general). The experimental magnetization and the nanoparticle magnetization are allowed to decrease with temperature following a spin wave-like behaviour[8] "Bloch type law" as:

$$M(T) = M(0)e^{-BT^{3/2}} \qquad (4)$$

the Bloch constant (B) is obtained from the magnetization measurements as a function of temperature under the maximum field of 7 T, being between 2 and 4×10^{-5} in all cases. It is important to note that the anisotropy constant K is dependent of the temperature and it has to be taken into account to calculate the value.[9]

All the mentioned fittings are represented in Figure S6 (black curves).

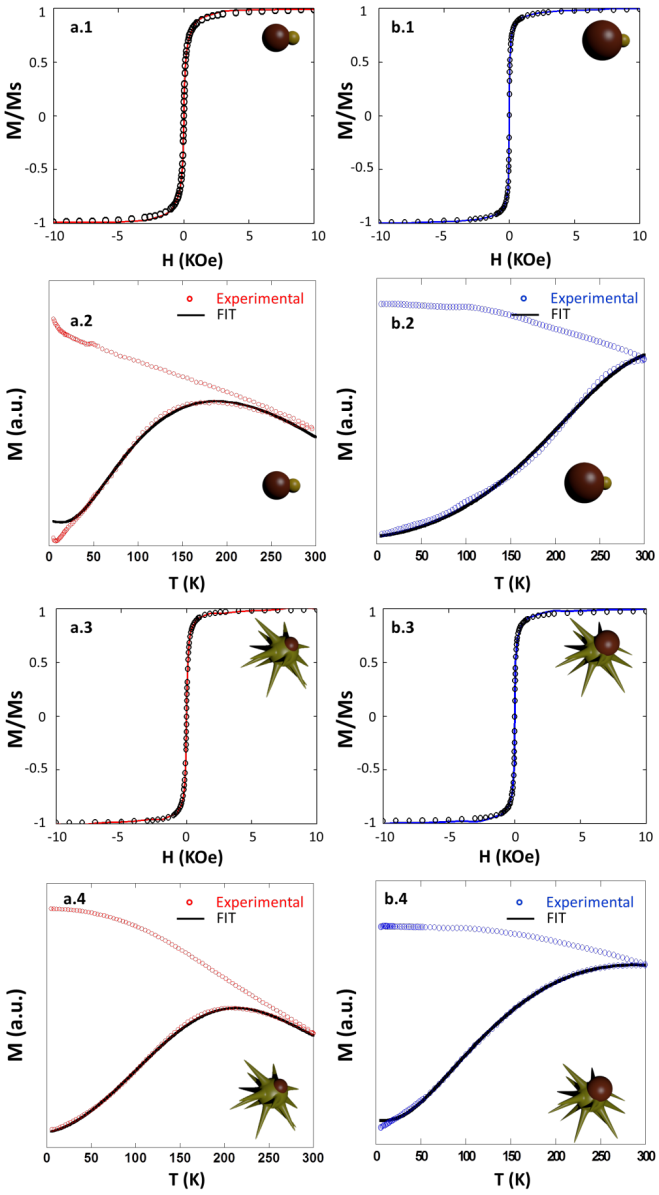

Figure S7: Magnetic characterization of nanodumbbells (ND.16 and ND.20) and JMNSs (JMNS.16.25 and JMNS.20.41) showing hysteresis loops and ZFC-FC. Fittings of both measurements are represented by black lines.

5 MRI characterization

5.1 MRI relaxation times vs. concentration

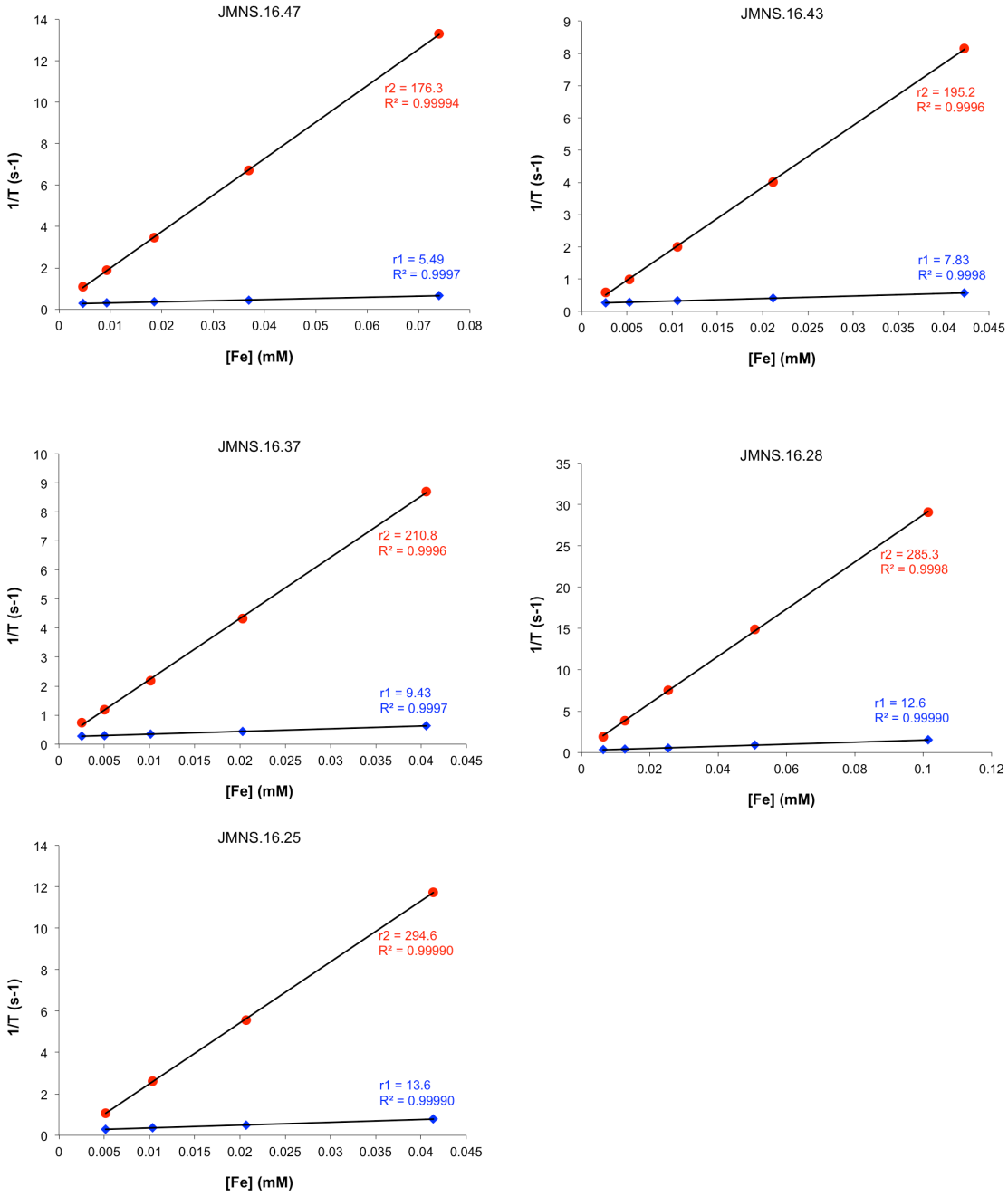

Figure S8: Relaxation constants (1/T2 and 1/T1) as a function of iron concentration for the different JMNSs with a 16 nm iron oxide part. The black lines show the linear fittings of the different plots. The slope (relaxivity) and the coefficient of determination are expressed for every fitting.

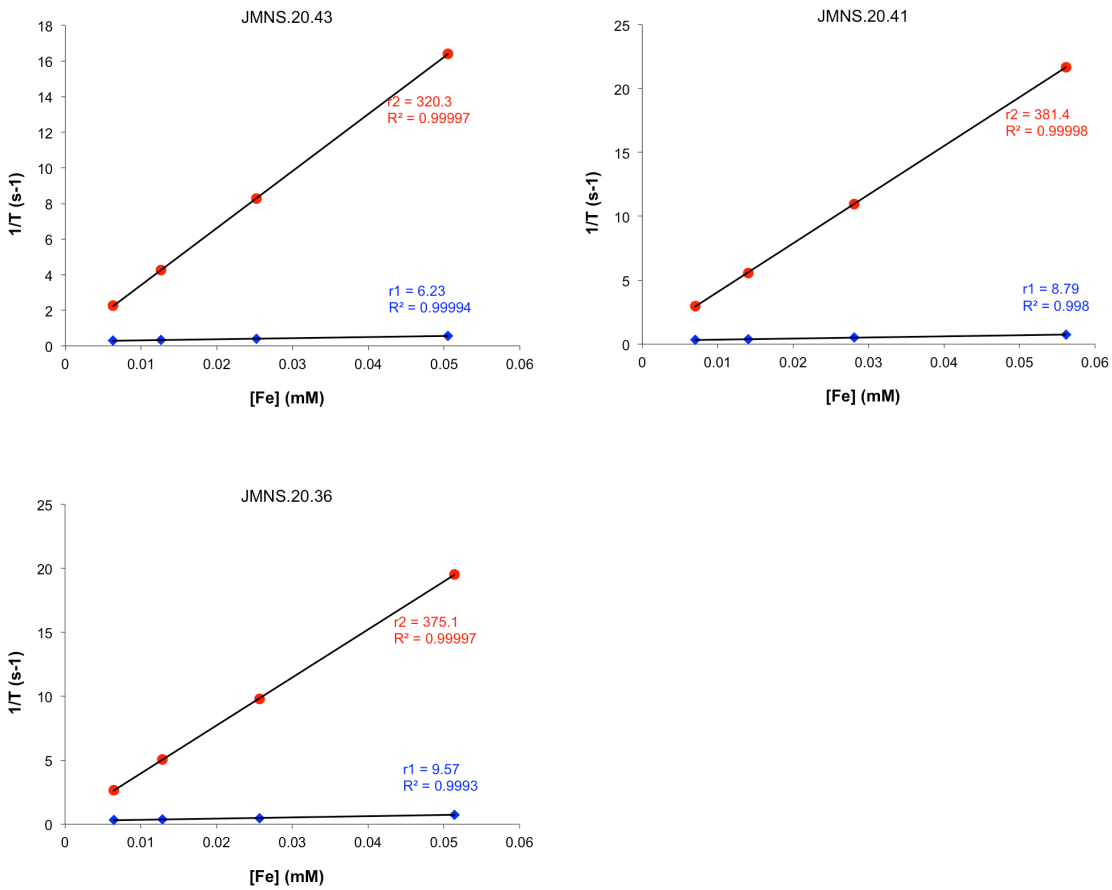

Figure S9: Relaxation constants (1/T2 and 1/T1) as a function of iron concentration of the different JMNSs with a 20 nm iron oxide part. The black lines show the linear fittings of the different plots. The slope (relaxivity) and the coefficient of determination are expressed for each fitting.

5.2 r1 and r2/r1 graph

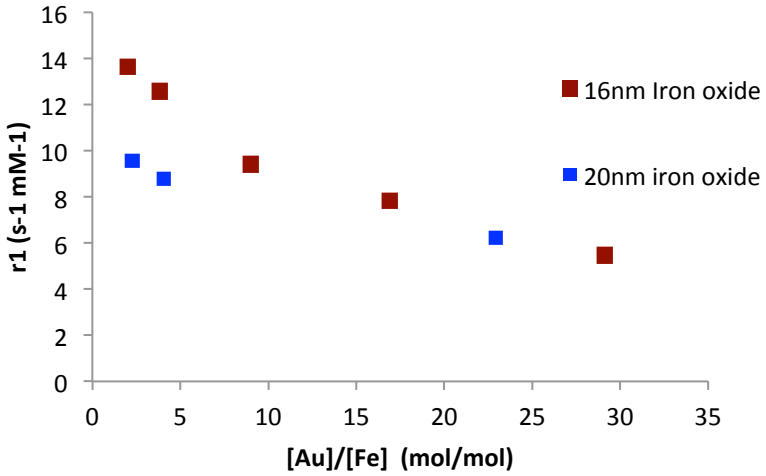

Figure S10: r1 relaxivity of JMNSs with 16 nm (brown symbols) and 20 nm (blue symbols) iron oxide parts.

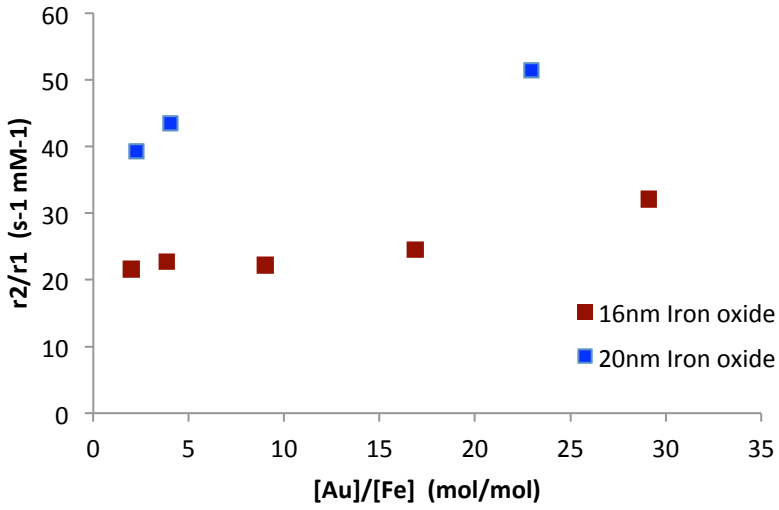

Figure S11: r2/r1 relaxivity of JMNSs with 16 nm (brown symbols) and 20 nm (blue symbols) iron oxide parts.

6 CT attenuation pots

The experiments were performed starting with a highly concentrated solution, which was then successively diluted. The contrast efficiency was obtained by the slope after a regression line to a $y = ax$ function. The graphs below represent the attenuation plots for every sample at three different energies.

JMNS.16.47

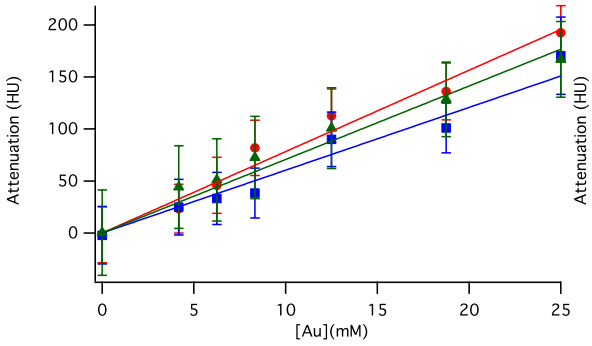

JMNS.16.43

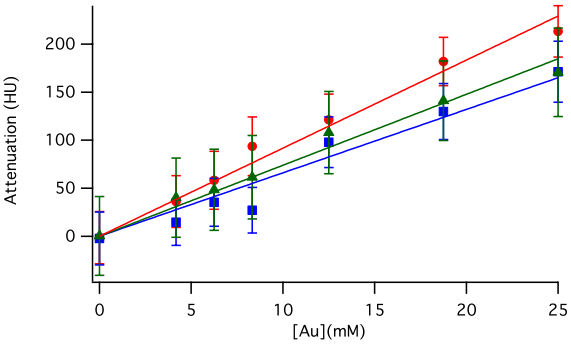

JMNS.16.37

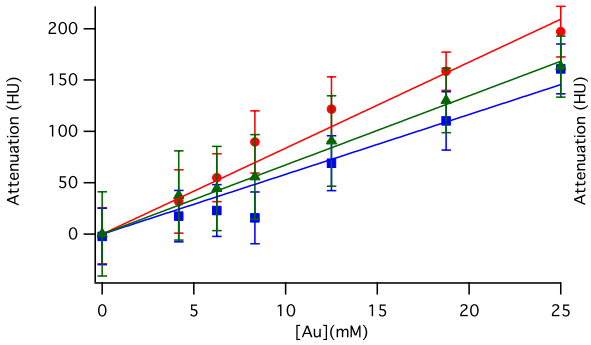

JMNS.16.28

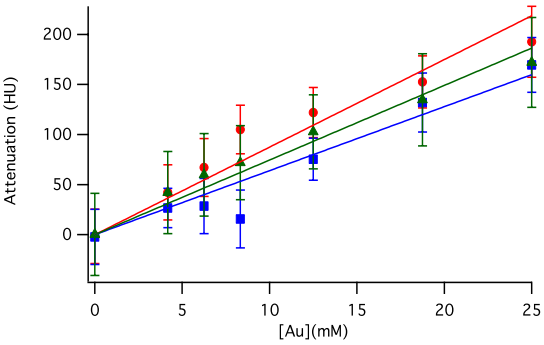

JMNS.16.25

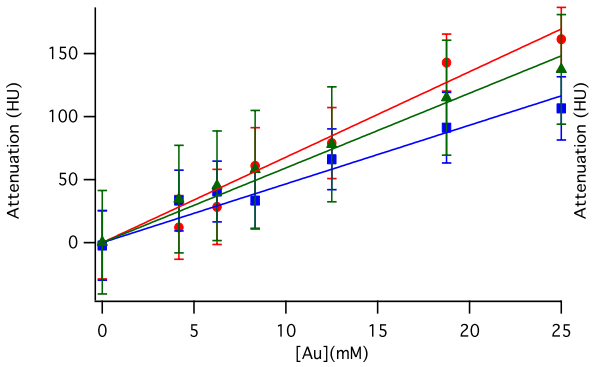

JMNS.20.43

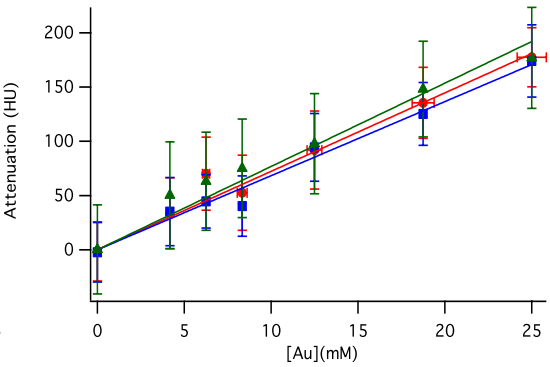

JMNS.20.41

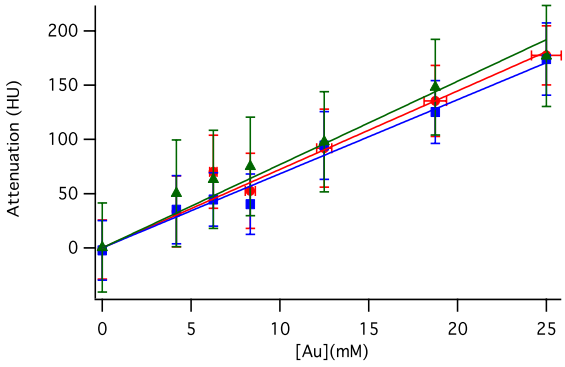

JMNS.20.36

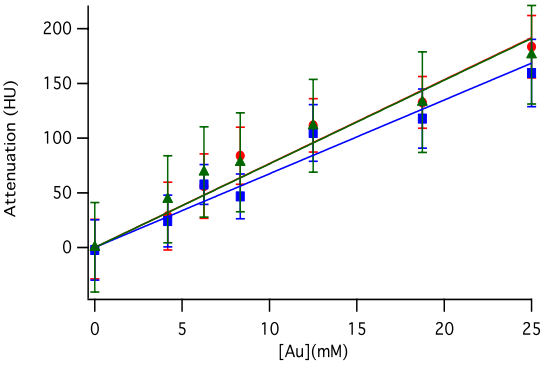

Figure S12: CT attenuation experiments using 16 nm and 20 nm iron oxide JMNSs at three different energies (70 KeV, red circles; 80 KeV, blue squares; 100 KeV, green triangles).

7 Optical imaging

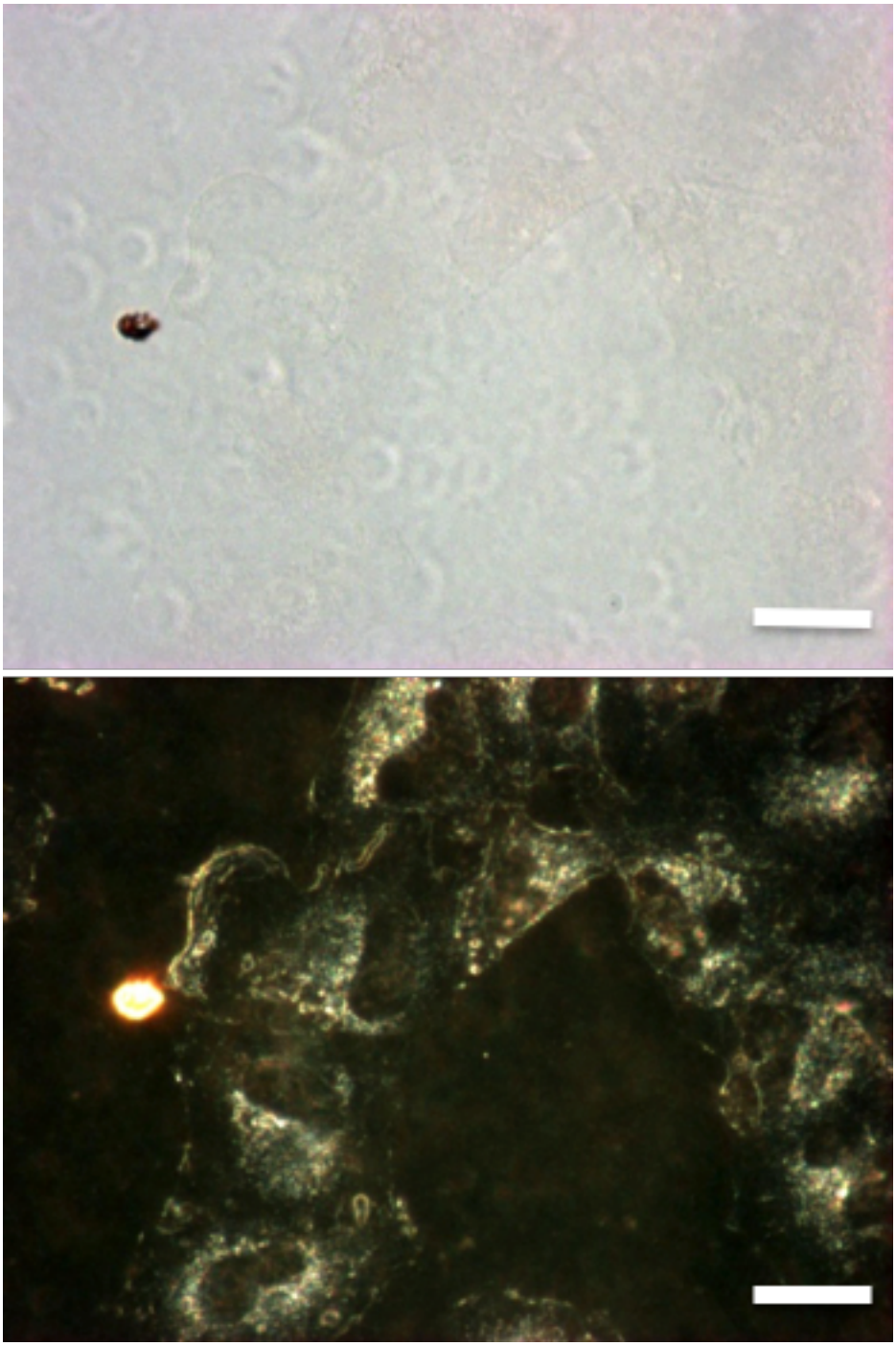

Figure S14: Control experiments showing a lack of Prussian blue staining (top) or scattered light (bottom), imaged using bright-field and dark-field microscopy respectively, after treatment of A549 cells with media alone, and thereafter stained and imaged using the same methods as for cells incubated with JMNSs. The lack of Prussian blue staining and scattered light confirms the specificity of both techniques for the visualization of iron oxide and gold respectively.

8 References

1. J. F. Moulder, W. F. Stickle, P. E. Sobol and K. D. Bomben, *Handbook of X Ray Photoelectron Spectroscopy* Physical Electronics, 1995.
2. M. Descostes, F. Mercier, N. Thromat, C. Beaucaire and M. Gautier-Soyer, *Appl. Surf. Sci.*, 2000, **165**, 288-302.
3. I. Castellanos-Rubio, M. Insausti, E. Garaio, I. Gil de Muro, F. Plazaola, T. Rojo and L. Lezama, *Nanoscale*, 2014, **6**, 7542-7552.
4. M. Knobel, W. C. Nunes, L. M. Socolovsky, E. De Biasi, J. M. Vargas and J. C. Denardin, *J. Nanosci. Nanotechnol.*, 2008, **8**, 2836-2857.
5. R. Kaiser and G. Miskolczy, *J. Appl. Phys.*, 1970, **41**, 1064-1072.
6. J. B. Weaver, A. M. Rauwerdink and E. W. Hansen, *Med. Phys.*, 2009, **36**, 1822-1829.
7. E. C. Stoner and E. P. Wohlfarth, *Phil. Trans. R. Soc. A*, 1948, **240**, 599-642.
8. R. Aquino, J. Depeyrot, M. H. Sousa, F. A. Tourinho, E. Dubois and R. Perzynski, *Phys. Rev. B*, 2005, **72**, 184435.
9. C. Zener, *Phys. Rev.*, 1954, **96**, 1335-1337.